Supporting Information

Efficient removal of sulfonamides in complex aqueous environments by N, P-co-doped graphitic biochar: The crucial role of P_2O_5

Wei Tang [1, 2], Daniel S. Alessi [3], Tongshuai Wang [1, 2, 4], Jingqi Wu [1, 2], Shijia Li [1, 2], Kurt Konhauser [3], Zhixiong Li [1, 2], Jiawei Chen [1, 2*]

[1] State Key Laboratory of Biogeology and Environmental Geology, China University of Geosciences, Beijing 100083, P. R. China

[2] School of Earth Sciences and Resources, China University of Geosciences, Beijing 100083, P. R. China

[3] Department of Earth and Atmospheric Sciences, University of Alberta, Edmonton, Alberta T6G 2E3, Canada

[4] China Household Electric Appliance Research Institute (CHEARI), Beijing 100053, P. R. China

[*]Corresponding Author

Email: chenjiawei@cugb.edu.cn

Phone: 86-10-82321959

Submission: December 2, 2023

Supplementary materials and methods

Text S1 Chemical and reagent

Sulfapyridine (SPY, $C_{11}H_{11}N_3O_2S$, 98.0%), sulfadiazine (SDZ, $C_{10}H_{10}N_4O_2S$, 98.0%), sulfamethoxazole (SMX, $C_{11}H_{11}N_3O_2S$, 98.0%), sulfathiazole (STZ, $C_9H_9N_3O_2S_2$, 98.0%), peroxodisulfate ($Na_2S_2O_8$, PDS, 99.0%), potassium iodide (KI, 99.0%), potassium bromide (99.9%), l-histidine ($C_6H_9N_3O_2$, 99%), humic acid (HA, ≥90%) and sodium nitrate ($NaNO_3$, 99.5%) were purchased from Macklin Biochemical (Shanghai, China). Phosphoric acid (H_3PO_4, 99.9%), Methanol (MeOH, 99.9%) and acetonitrile (99.9%) were purchased from ANPEL Laboratory Technologies Co. (Shanghai, China). Other reagents were provided by Sinopharm Chemical Reagent Co. Ltd. (China). Deionized (DI) water (>18.3 MΩ·cm) was used throughout the experiments. SPY was dissolved in methanol to prepare the stock solution (2 g L^{-1}) and the methanol in the working solutions was kept below 0.1% to exclude the co-solvent effect. The actual surface water was taken from a slow-flowing area, the Qing River, Beijing (40°1'8.549" N, 116°17'4.248" E).

Text S2 Preparation of biochar and another common catalyst

Corn stalks sourced from Fuping, Shanxi, China were chosen as the precursor for the biochar. The corn stalks were washed with deionized water (DIW, >18.3 MΩ·cm), dried, and ground into a fine powder with a size less than 1.0 mm. Briefly, the biomass was mixed with ammonium polyphosphate (APP) at various mass ratios, followed by pyrolysis at a constant temperature (300~900 °C) for 2 hours, with a heating rate of 5

°C min^{-1} under a nitrogen atmosphere. After natural cooling, the pyrolysis product was washed three times with DIW to remove any loss-prone N and P from the biochar surface. It was then oven-dried at 80 °C for 12 hours and ground into a powder using 35 mesh sieves (0.5 mm). The synthesized products were named NPBCX, where X represents the pyrolysis temperature. To serve as a control group, pristine biochar BC900 was prepared at the peak temperature of 900 °C.

Fe_3O_4, Mn_2O_3, Fe_2O_3 were purchased from Macklin Biochemical (Shanghai, China). H_3PO_4@BC900: Phosphoric acid-modified graphite biochar; KOH@BC900: Potassium hydroxide--modified graphite biochar; NBC900: Nitrogen-doped graphite biochar (Nitrogen source: urea); Fe@BC900: Magnetic graphite biochar; Fe@NBC900: Nitrogen-doped magnetic graphite biochar; ONPBC900: Preoxidized nitrogen and phosphorus co-doped graphite biochar.

Text S3 Biochar characterization

The scanning electron microscope (SEM-EDS; Zeiss Supra 55-VP, Heidenheim, Germany) with elemental mapping was applied to observe the morphological and compositional changes of the biochars. The specific surface area, pore volume, and average pore diameter of the biochar samples were obtained by analyzing the N_2 adsorption-desorption isotherms (Quadrasorb Station 1 analyzer, Quantachrome Instruments, Boynton Beach, USA) based on the Brunauer-Emmett-Telle (BET) and Barrett-Joyner-Halenda (BJH) theories. Zeta potential analyzer (Nanobrook ZetaPlus-

Brookhaven Instuments, Holtsville, USA) was used to determine the zeta potential of the samples in aqueous solution with different pH value.

The physicochemical properties of the pristine biochars and N, P-co-doped biochar samples were characterized using multiple advanced spectroscopic techniques. The bulk elemental composition (C, H, N, and S) was determined by an elemental analyzer (EA3000, Euro Vector, Pavia, Italy). The ash content was obtained from the mass difference after samples heated in a muffle furnace at 750 °C for 4 h. The bulk O content was calculated by subtracting the CHNS and ash contents from the total dry weight. The surface functional groups of biochar samples were detected by the Fourier-transform infrared spectroscopy (FTIR; Nicolet iS10, Thermo Fisher Scientific, Waltham, USA) and X-ray photoelectron spectroscopy (XPS, ESCALAB 250Xi, Massachusetts, USA).

The XPS spectral deconvolution was separately for C 1s, N1s and P 2p. C 1s spectrums have been installed in four peaks with binding energies from 284.5 ± 0.2, 285.6 ± 0.2, 286.5 ± 0.2 and 288.6 ± 0.3 eV, which corresponded to C=C, C-OR, C=O and -COOR, respectively (Tang et al., 2021). The N1s spectra had 4 peaks of 398.2 ± 0.2, 399.9 ± 0.1, 401.2 ± 0.2 and 404.0 ± 0.3 eV, which corresponded to pyridinic N, graphitic N, pyrrolic N and oxidized N, respectively (Pang et al., 2022). The P 2p spectra showed the peaks at 132.2 ± 0.1 eV (PO_4^{3-}), 133.1 ± 0.1 eV ($P_2O_7^{4-}$), 134.2 ± 0.1 eV (PO_3^-) and 136.0 ± 0.6 eV (P_2O_5), respectively (Shih et al., 1999, Huang et al., 2014).

Electrochemical measurements were performed on an electrochemical workstation (CHI660e) with a three-electrode cell. The structure composition of biochar samples was examined by X-ray diffraction (XRD) using a D/Max 2500 (Rigaku, Japan) with a Cu-Kα radiation in the range of 10-90° (2θ). To identify the graphite structure, the position and intensity of peaks in the observed XRD patterns were compared with the powder diffraction files (PDF, 2004) provided in the software MDI Jade 6.0. Similarly, the Raman spectrum shift (Renishaw Raman spectrometer, UK) was used to evaluate the disordered carbon structure and graphitic crystallites of the biochar samples.

Text S4 Detailed procedure for EPR test

The electron paramagnetic resonance (EPR) spectra were obtained using an EMX10/12 spectrometer (EMX10/12, Bruker, Germany). The applied instrumental conditions were as follows: resonance frequency of 9.82 GHz, microwave power of 20.07 mW, modulation frequency of 100 kHz, modulation amplitude of 1.0 G, sweep width of 100 G, time constant of 40.96 ms, sweep time of 83.93 s, and receiver gain of 2.0×10^4 at room temperature. In the sample vials, 150 mM 5,5-dimethyl-1-pyrroline-N-oxide (DMPO) or 2, 2, 6, 6-tetramethyl-4-piperidinol (TEMP) was added as the spin-trapping agent in a buffer solution (pH=7.4, 20 mM phosphate). Peak intensities of the DMPO–SO_4, DMPO–OH, and TEMPN signals at 5 min were applied as indexes of the generated ROS after the correction of background noise.

All EPR scanning was repeated in triplicate and the sum value was output for G factor calculation. The raw data of the EPR signal (arbitrary units) was processed through the cwEsr software (3.3.36E XB version) provided by JEOL for directly reading the G factors, which were calculated based on the equation $h \cdot f = g \cdot m_B \cdot B$, where h, f, m_B , and B signify Planck's constant equal to 6.62×10^{34} J·s, applied microwave frequency, Bohr Magneton (9.27×10^{-27} J/mT), and magnetic field strength, respectively. Specifically, the constant mass (15 mg) of biochar was added into a micro-pipette, following placed in the detector for recording signal. The parameters of EPR experiments were set as follows: center field 3460 G, sweep width 100 G, microwave frequency 9.71 GHz, microwave power 19.71 mW, modulation frequency 100 kHz, modulation amplitude of 1.0 G, and sweep time of 83.97 s.

Text S5 Detailed procedure for electrochemical test

A carbon paper electrode loaded with NPBC powder was first prepared. Nafion® solution (5.0 wt%, 0.2 mL) and NPBC powder (20 mg) were mixed with ethanol (2 mL), then ultrasonic dispersion for 3 h to form a suspension solution. Next, 20 μL suspension was dropped onto the surface of the carbon paper electrode. The carbon paper electrode was vacuum dried at 60 °C for 8 h. Silver/silver chloride electrode (Ag/AgCl) and Pt wire electrode were used as reference electrode and counter electrode, respectively. Electrochemical impedance spectroscopy (EIS) was carried out at open potential in 50 mM Na_2SO_4 solution, and the frequency was in the range from

10^5 to 10^{-1} Hz. Linear sweep voltammetry (LSV) was measured at the potential from 0.0-1.5 V (vs. Ag/AgCl) with a scanning rate of 50 Mv s^{-1}. Chronoamperometries were carried out at the bias of 0.0 V (vs. Ag/AgCl) with 50 mM Na_2SO_4 as supporting electrolyte.

Text S6 Detailed procedure for adsorption study

For adsorption kinetics, SPY at an initial concentration of 20 mg·L^{-1} was mixed with 0.05 g BC900 or NPBC900-2:1.1 in 500 ml of 0.01 M $NaNO_3$ in a bottle. Under shaking at 180 rpm and 25 °C, about 1 mL supernatant was withdrawn at interval time of 0, 0.17, 0.5, 1.0, 2.0, 4.0, 8.0, 12, 24, 32, 36, 48, 60, 72 h. The adsorption isothermal experiments were performed in 15 mL bottles by mixing 1 mg BC900 or NPBC900-2:1.1 with 10 mL 0.01 M $NaNO_3$ as the base solution containing SPY with the concentration of 2.5~50 mg·L^{-1}. All the bottles were sealed with Teflon-lined screw plugs and stirred at 180 rpm at an ambient temperature of 25 °C for 72 h, under the steady-state time listed in kinetic experiments (Fig. S13a). The bottles were placed in solid-liquid separation, and approximately 2 mL of supernatant was removed, filtered with a 0.22-μm polyether sulfone filter and added to the 2 mL vials for SPY analysis. All the batch experiments were run in triplicate and the SPY uptake by biochar was calculated by mass balance. The blank and control test indicated the loss of SPY was negligible during the experiments.

The sorption capacity for SPY onto biochar was calculated using Eq. (S1).

$$Q_e = \frac{(C_i - C_e) * V}{W_{BC}} \quad \text{(S1)}$$

- where Q_e (mg·g$^{-1)}$ is the amount of adsorbed SPY on biochar at equilibrium; C_i (mg·L^{-1}) is the initial concentration of SPY; C_e (mg·L^{-1}) is the equilibrium concentration of SPY in the solution; V is the volume of aqueous solution (mL); W_{BC} is the weight of the biochar (g).

The quasi first-order and second-order kinetic models in the following Eq. (S2) and (S3) could describe such sorption behavior.

Quasi first-order kinetic model: $Q_t = q_1(1 - exp(-k_1 t))$ (S2)

Quasi second-order kinetic model: $Q_t = \frac{t}{(1/k_2 q_2^{\,2}) + (t/q_2)}$ (S3)

– where q_1 and q_2 (mg·kg^{-1}) is the adsorption capacity at equilibrium; Q_t (mg·kg^{-1}) is the adsorption capacity for SPY on biochars at time t; k_1 (min^{-1}) is the equilibrium rate constant of quasi first-order; k_2 (kg·mg^{-1}·min^{-1}) is the quasi second-order rate constant.

The Langmuir and Freundlich Isothermal adsorption model in the following Eq. (S4) and (S5) could describe such sorption behavior.

Langmuir Isothermal adsorption model: $Q_e = \frac{Q_m b C_e}{1 + bC_e}$ (S4)

Freundlich Isothermal adsorption model: $Q_e = K_f C_e^n$ (S5)

- where Q_e (mg·g$^{-1)}$ is the amount of adsorbed SPY on sorbents at equilibrium; C_e (mg L^{-1}) is the equilibrium concentration of SPY; b (L mg^{-1}) is the sorption affinity parameter in Langmuir model; Q_m (mg·g^{-1}) is Langmuir saturated sorption capacity; K_f (mg^{1-n}·g^{-1}·L^n) is the Freundlich sorption parameter and n is the nonlinearity factor, indicating the sorption intensity.

Text S7 Operation details of HPLC

The SPY in solution was measured by HPLC (LC-20AD, Shimadzu, Kyoto, Japan) equipped with a reversed-phase C18 analytical column (5 μm, 4.6 mm × 250 mm). The mobile phase was acetonitrile and 0.5% phosphoric acid with a ratio of 20:80 (v:v). The conditions were optimized as the flow rate of 1 $mL \cdot min^{-1}$, the detection wavelength 254 nm, the column temperature 35 °C, and the injection volume 10 μL. The retention time of SPY was 4.6 min.

The SDZ in solution was measured by HPLC (LC-20AD, Shimadzu, Kyoto, Japan) equipped with a reversed-phase C18 analytical column (5 μm, 4.6 mm × 250 mm). The mobile phase was acetonitrile and DIW with a ratio of 10：90 (v:v). The conditions were optimized as the flow rate of 1 $mL \cdot min^{-1}$, the detection wavelength 275 nm, the column temperature 35 °C, and the injection volume 10 μL. The retention time of SDZ was 12 min.

The SMX in solution was measured by HPLC (LC-20AD, Shimadzu, Kyoto, Japan) equipped with a reversed-phase C18 analytical column (5 μm, 4.6 mm × 250 mm). The mobile phase was acetonitrile and 0.1% formic acid with a ratio of 30:70 (v:v). The conditions were optimized as the flow rate of 1 $mL \cdot min^{-1}$, the detection wavelength 265 nm, the column temperature 30 °C, and the injection volume 20 μL. The retention time of SMX was 10 min.

The STZ in solution was measured by HPLC (LC-20AD, Shimadzu, Kyoto, Japan)

equipped with a reversed-phase C18 analytical column (5 μm, 4.6 mm × 250 mm). The mobile phase was acetonitrile and 0.5% phosphoric acid with a ratio of 20:80 (v:v). The conditions were optimized as the flow rate of 1 $mL \cdot min^{-1}$, the detection wavelength 283 nm, the column temperature 35 °C, and the injection volume 10 μL. The retention time of STZ was 6 min.

Text S8 Operation details of ESI-MS

The LC separation was carried out on a waters Symmetry C18 column (3.5 μm, 2.1mm I.D.×150 mm). Elution was performed at a flow rate of 0.25 $mL \cdot min^{-1}$ with H_2O containing 0.1% (v/v) formic acid as eluent A and acetonitrile containing 0.1% (v/v) formic acid as eluent B, employing a linear gradient from 10% B to 15% B in 5~8 min, 15% B to 40% B in 8~13 min, 40% B to 90% B in 13~18min, 90% B to 10% B in 13~26 min, 10% B to 0% B in the next 4 min. MS analysis was carried out in positive mode using electrospray ionization (ESI) source. Instrument parameters were as follows: capillary voltage 3.8 kV, fragmentor 125 V, desolvation gas (nitrogen, ≥ 99.995%) flow 10 $L \cdot min^{-1}$, temperature 305 °C, nebulizer pressure 30.0 psi (2.76 bar), and nitrogen (≥ 99.999%) was used as collision gas. The mass analyzer was operated in full scan mode (m/z range 50-350) in order to identify the products.

Text S9 Detailed procedure for phytotoxicity assay

The phytotoxicity of SPY and its degradation byproducts was measured by the Chinese cabbage seeds (*Brassica chinensis* L.) growth inhibition assay. Firstly,

sterilized filter papers were placed in Petri dishes and added 7 mL of deionized water. Approximately 120 Chinese cabbage seeds were placed in each petri dish and incubated 24 h in a dark at 25 °C Twenty of uniform-germinated seeds were selected and moved to each Petri dish with 7 mL of the samples (DIW, SPY, PDS, treated SPY solution). Then, these Petri dishes were placed in the growth chamber and incubated in the dark for 4 days at 25 °C. All the samples were tested in triplicate. The length of the seedling root was used to measure the toxic effects of different conditions on Chinese cabbage. The negative control was deionized water, where the mean length of the root was labeled as L_0. The positive control was the original SPY and the mean length of roots of other groups were labeled as L.

Text S10 Detailed analysis for NPBC synthesized with different mass ratios of biomass and APP

XPS analysis was conducted for the roles of C 1s, N 1s and P 2p as well as the surface chemical composition of NPBC (Figs. S3-S5, Table S5). The identification of the C 1s, N 1s, and P 2p was undertaken in details (Text S3). XPS spectra of C 1s and FTIR spectra revealed that NPBC900 (2:1.1) had sufficient adsorption affinity towards SPY, as indicated by the relatively high contents of C-OR and -COOR (Fig. S7, S11), which favored local attraction of SPY for degradation. According to Fig. S5, a higher quantity of edge nitrogen (pyrrole N and pyridine N, 57.07%) on the surface of NPBC900 (2:1.1) was found, and it would form more surface-active complexes, enhancing the catalytic activity. Meanwhile, the correlation analysis ($p < 0.01$) between

P_2O_5 and C_t/C_0 was performed (Fig. 2). The positive correlation indicated that the P_2O_5 content was critical due to that P atoms play an important role in the formation of $^1O_2$ and directly enhance the removal of SPY (Deng et al., 2023). Besides $^1O_2$ and surface-active complexes, the graphitic structure and defective degree of carbon materials are often the key factors in AOPs. Thus, XRD and Raman measurements were performed on NPBC (Fig. S3a, b).

The XRD pattern (Fig. S3a) showed two peaks at 26.5° and 40.4° (2θ), corresponding to the (002) and (100) planes of amorphous carbon and crystalline carbon, respectively. Despite according to Fig. S5, NPBC900 (2:1.1) contains relatively low graphite N contents, the high crystallization peak of NPBC900 (2:1.1) indicate its overall high degree of graphitization, which could enhance the electron transfer. Thus, the electron transfer might be one of the primary mechanism for SPY removal. In addition, a pair of characteristic peaks (D and G peaks) in Raman spectra (Fig. S3b) are associated with an imperfect and well-defined carbon structure, and ID/IG ratios can unveil the defective degree of NPBC. The similar values of ID/IG indicated the defects were relatively close, and this was not the primary mechanism for removing SPY.

Text S11 Detailed analysis for NPBC synthesized with different temperature

The XPS spectra of C 1s and the FTIR spectra demonstrated that NPBC900 exhibited the highest adsorption affinity towards SPY, attributed to its highest content of C-OR and -COOR (as shown in Fig. S10 and S11). As a result, NPBC900 was able

to facilitate more SPY aggregation for efficient degradation. And Fig. 1d showed that NPBC700 had the highest N and P contents, while the corresponding SPY removal efficiency was not ideal. This again illustrates the critical role of the species form of heteroatoms in AOPs, rather than their total content. Additionally, the high surface nitrogen content of NPBC900 (Fig. S10), specifically pyrrole N and pyridine N, resulted in the formation of surface-active complexes, enhancing the catalytic reactivity.

And the graphitic structure and defective degree of NPBC were characterized by XRD and Raman techniques (Fig. S3c, d). The highest intensity of crystallization peak indicated the highest degree of graphitization in NPBC900, which could provide stronger electron transfer ability to AOPs. Fig. S3d displayed the Raman spectrums of NPBC synthesized at high pyrolysis temperature. It showed the ID/IG value increased from 0.86 to 0.98 as the pyrolysis temperature increased from 600 to 900 °C, indicating that more defects were generated during heat treatment. This is because the pyrolysis process is able to convert biomass into biochar by condensing smaller organic molecules into conjugated aromatic rings, which generates defective edges with hydrogen and oxygen functional groups (Guizani et al., 2017). The numerous defects present in NPBC synthesized at 900 °C pyrolysis temperature acted as highly active sites, greatly enhancing the activation of PDS and promoting SPY removal. Additionally, higher levels of defects in the carbon framework can also accelerate electron transfer, thereby improving catalytic performance.

Text S12 Adsorption of SPY on NPBC900

Fig. S13a showed that the adsorption, and desorption reached a preliminary equilibrium after 60 minutes. From Fig. S13b, the SPY adsorption capacity of NPBC900 (Q_m=35.14 ± 2.01 mg·g^{-1}) was higher than that of BC900 (Q_m=27.31 ± 1.84 mg·g^{-1}). The adsorption kinetics was investigated by quasi-first order and quasi-second order models (Fig. S13a). Table S2 showed that the quasi-second order model (R^2=0.982~0.987) fits the experimental data better than the quasi-first order model (R^2=0.936~0.936), suggesting that the adsorption of SPY on NPBC900 was mainly chemical adsorption rather than physical process (Ding et al., 2013). Herein, Langmuir and Freundlich adsorption models were used to analyze the adsorption isotherm of SPY on NPBC900 (Fig. S13b). From the calculated model parameters (Table S5), the Langmuir model (R^2=0.990~0.996) fits better than the Freundlich model (R^2=0.950~0.975), indicating the dominated monolayer adsorption (Parab and Sudersanan, 2010). Hence, the adsorption mechanism of SPY on NPBC900 was attributed to a chemical monolayer adsorption dominated by the surface active sites and H-bonding. Notably, after N and P doping, the adsorption of SPY on NPBC900 was slightly higher than that on BC900. The reason may be explained by the higher (O+N)/C ratio, larger specific surface area (SSA) and lower V_{mic} compromise of NPBC900.

The SSA of NPBC900 increased to 605.85 m^2 g^{-1} in comparison with BC900 (366 m^2 g^{-1}), probably due to the developed porous structures with the increase in total pore

volume (V_{tot}) from 0.328 to 0.374 cm^3 g^{-1} (Table S4). The number of micropores in NPBC900 decreased due to the development of some microporous structures into meso-pores (V_{mic}: 0.223 to 0.155 cm^3 g^{-1}). This phenomenon could be attributed to the thermal decomposition of the N, P source reagent (ammonium polyphosphate, APP), which would simultaneously release NH_3, N_2 or N_2O gases and adjust the porous structure of biochar. This could also be estimated from the N_2 adsorption-desorption curve of biochar (Fig. S13c). All the biochars exhibited the type I isotherm at low relative pressures, indicating large adsorption capacity and narrow hysteresis loops. They showed a rich porous structure with slightly higher relative pressure (Guo et al., 2018). The pore size distribution curve (Fig. S13d) showed that all the samples had multiple meso-pores with an average size of 2~2.5 nm. NPBC900 possessed a significantly higher meso-porous volume than BC900, indicating that it can promote rapid diffusion kinetics and enhance contact with organic pollutants or oxidants.

Text S13 Optimization of experimental parameters on SPY removal

Firstly, the effect of initial solution pH on SPY removal was investigated, and the activation experiments were performed at initial pH of 3.05, 4.98, 7.04, 9.00, and 11.02. (Fig. S17a). Surprisingly, the SPY removal rate can be maintained at a high level (95.54%-98.39%) regardless of whether the conditions are strongly acidic, neutral, or weakly alkaline (pH≈3-9). This result indicates that the NPBC900/PDS system has good adaptability in actual wastewater treatment. Even when the pH was adjusted to

11.02, the inhibition effect was not obvious. To be specific, 83.85% of SPY was removed, while the k_{obs} value (0.0125 min^{-1}) was 2.27-folds lower than that at pH=5 (0.0284 min^{-1}) (Fig. S18a). The reason for the decrease in SPY removal efficiency is that the activation of PDS was suppressed to some extent at pH=11 (Pang et al., 2022).

To further reveal the inhibitory effect at pH 11, the zeta potential of NPBC900 was investigated (Fig. S17b). The calculated zeta potential of NPBC900 was 3.91, which means that NPBC900 has a negative charge at pH > 3.91 and a positive charge at pH < 3.91. In addition, the pk_{a1} and pk_{a2} of SPY are 2.30 and 8.40 respectively (Gao et al., 2005). Thus, it could be concluded that the SPY is mainly present in three forms under different pH conditions, including cation (pH < 2.30), zwitterion (2.30 < pH < 8.40), and anion (pH > 8.40). Therefore, at the initial pH of 11.02, NPBC900 was negatively charged, and SPY molecules showed anionic forms. The electrostatic repulsion among the ternary systems of negatively charged NPBC900/SPY anionic/$S_2O_8^{2-}$, would suppress the interaction among them, weakening the SPY removal efficiency.

The amount of ROS generated was found to be dependent on the PDS dose, which played a crucial role in SPY removal. Therefore, optimization of the PDS dose was necessary (Fig. S17c). When a low dose of PDS (0.1 mM) was added, 75.59 % of SPY was removed within 120 min. By increasing the dosage of PDS to 0.5 mM, almost complete removal of SPY was observed within 120 min (98.21%), and the k_{obs} value (0.0311 min^{-1}) was 2.93 times higher than that at PDS=0.1 mM (0.0106 min^{-1}) (Fig. S18b). High PDS concentrations can produce high levels of ROS, which attack and

oxidize SPY, increasing the speed and effectiveness of the catalytic reaction. As the PDS dosage was increased from 0.5 mM to 0.9 mM, the efficiency of SPY removal decreased from 98.21% to 96.05%. This decrease may be attributed to the mutual quenching of excessive reactive species resulting from higher PDS concentrations (Liu et al., 2020). And the available active sites on the catalyst surface were nearly fully occupied, leading to limited production of ROS (Yin et al, 2019). Thus, the appropriate PDS dose of 0.5 mM was used to optimize the SPY removal conditions.

The removal efficiency of SPY showed a clear negative correlation with the initial SPY concentration, as shown in Fig. S17d. As the initial SPY concentration increased from 5 to 80 mg L^{-1}, the removal rate decreased from 100% to 59.13% within 120 min, and the corresponding k_{obs} value decreased from 0.1070 min^{-1} to 0.0032 min^{-1} (Fig. S17c). The decrease in SPY removal efficiency at high initial SPY concentrations could be attributed to two factors. Firstly, the active sites of NPBC900 were severely covered by the high concentration of SPY. Secondly, there was a shortage of ROS in the presence of excessive SPY. Despite the high SPY concentration of 80 mg L^{-1}, NPBC900 still demonstrated excellent removal ability, achieving a removal rate of 59.13%.

In addition, a lower catalyst dosage is not only more economical, but also more environmentally friendly. Fig. S17e illustrates the relationship between SPY removal and the amount of NPBC900 added. As expected, the efficiency of SPY removal increased proportionally with the amount of catalyst added. At a low catalyst dose (0.03

g L^{-1}), only 44.09% of SPY was removed. However, a substantial increase in SPY removal was observed when using 0.1 g L^{-1} NPBC900, where almost all SPY was removed within 120 min (96.98%). The kobs value (0.0280 min^{-1}) was also 7.0-folds higher than that at 0.03 g L^{-1} (0.0040 min^{-1}), as shown in Fig. S17d. The enhanced removal efficiency could be attributed to the higher catalyst dosage that may catalyze PDS to generate more ROS, leading to the oxidation of SPY. As the catalyst dosage was further increased from 0.1 g L^{-1} to 0.2 g L^{-1}, SPY was found to be completely removed within 120 min. It should be noted that a sudden decrease in SPY concentration occurred in the first five minutes. This was due to the interaction of adsorption and oxidation, and the pre-adsorption was favorable for the subsequent oxidation.

In addition to comparing the reported common AOPs activators by direct citation (Table S7), this study also purchased or prepared a series of catalysts based on some of the more popular catalyst reports in recent years. As shown in Fig. S17f and S18e, for metal catalysts (Fe_3O_4, Mn_2O_3, Fe_2O_3), only about 3% SPY removal (K_{obs}=0.0002 min^{-1}) was observed under the conditions (initial SPY=20 mg L^{-1}, PDS=0.5 mM and catalytic=0.1 g L^{-1}). When biochar was introduced, more SPY was removed by Fe@BC900 (50.77%, K_{obs}=0.0017 min^{-1}). However, this was lower than the SPY removal efficiency of Fe@NBC900 (70.71%, K_{obs}=0.0080 min^{-1}). This is because both the iron species and the doped N acted as active catalytic sites. The graphitic structure of the catalyst was also beneficial for the activation of PDS (Li et al., 2020). While the

removal rate of Fe@NPBC900 (37.73%, Kobs=0.0026 min^{-1}) was lower than that of Fe@NBC900. This is because, unlike NBCs synthesized from urea, the pH of NPBC synthesized from APP is acidic, and most of the iron ions cannot exist on NPBC for a long time (Tang et al., 2021). Compared with other catalysts (H_3PO_4@BC900, KOH@BC900, NBC900 and ONBC900), NPBC900 brings great $^1O_2$ production capacity due to the successful introduction of N and P elements. What's more, it has more graphite and active site structure at the same mass. Thus, it can remove more SPY (98.33%, K_{obs}=0.0341 min^{-1}).

Text S14 Detailed for Quenching experiments

tert-Butanol (TBA) was used as a quencher of ·OH, as evidenced by a higher reaction rate constant with ·OH (k = 3.8–7.6 ×10^8 M^{-1} s^{-1}) than that of $SO_4^{\cdot -}$ (k = 4.0–9.1 ×10^5 M^{-1} s^{-1}). Methanol (MeOH) was considered to be a scavenger of both ·OH and $SO_4^{\cdot -}$, because it had an identical reaction rate with ·OH (k = 1.2–2.8 ×10^8 M^{-1} s^{-1}) and $SO_4^{\cdot -}$ (k = 1.6–7.8 ×10^8 M^{-1} s^{-1}). As depicted in Fig. 4f and S19e, a slight inhibition effect occurred on the 500 mM TBA/PDS and 500 mM MeOH /PDS, the TBA/PDS was more restrained (from 88.41% to 83.78%) and the k_{obs} value further decreased from 0.0155 min^{-1} to 0.0132 min^{-1}, indicating that $SO_4^{\cdot -}$ were more less involved in the reaction than ·OH, and ·OH might play the subordinate contribution in SPY removal. It's worth noting that the addition of 100 mM Furfuryl alcohol (FFA) and 10 mM L-histidine (L-His) exhibited a significant inhibitory effect, especially for 100

mM FFA (from 98.33% to 77.05% and 40.10%). Considering that they were the common quenchers of $^1O_2$ due to the $k_{FFA} = 1.2 \times 10^8\ M^{-1}\ s^{-1}$ and $k_{L\text{-}His} = 1.5 \times 10^8\ M^{-1}\ s^{-1}$. Therefore, $^1O_2$ was the main active substance in SPY removal. In addition, p-Benzoquinone (BQ) was the typical scavenger of $O_2^{\cdot -}$. When 10 mM BQ was added, the SPY removal rate decreased to 70.77% (k_{obs}=0.0063 min^{-1}). The strong inhibitory effect induced by BQ implied that $O_2^{\cdot -}$ should be produced in the NPBC900/PDS system. Similarly, the introduction of 10 mM KI effectively prevented the removal of SPY (dropped to 75.41%), suggesting that the surface-bound reactive species were also involved in the removal of SPY.

Text S15 SPY degradation pathways

Firstly, the active species attacked the C-N bond of SPY to produce P1 (m/z = 235). Then, P2 (m/z = 159) was generated by cleavage of the C-S bond. Subsequently, the P3 (m/z = 95) was generated by the same process. Secondly, the P4 (m/z = 186) was generated by SO_2 extrusion of SPY. The active species then attacked the C-N bond of P4 to produce P3 (m/z = 95) and P5 (m/z = 93). Thirdly, the formation process of P6 (m/z = 266) was generated by the electrophilic substitution of hydroxyl radicals in SPY. Subsequently. Then, P7 (m/z = 264) and P9 (m/z = 282) were generated by hydrogen abstraction and electrophilic substitution of hydroxyl radicals, and P8 (m/z = 190) and P3 (m/z = 95) were generated by N–S bond cleavage and hydroxylation. Fourthly, the P4 (m/z = 186) was generated by hydroxyl substitution of SPY. And then with the SO_2

extrusion and cleavage of the C-C bond of P4, thus P3 (m/z = 95) and P11 (m/z = 94) were produced. Fifthly, the active species attacked the N–C–N bond of SPY to produce P12 (m/z = 173). Next, the -NH_2 was continuously replaced by -OH to give P13 (m/z = 174) and P14 (m/z = 175). Then, the C-S is cleaved by the attack to give P11 (m/z = 94). Finally, these relatively small molecules were almost further oxidized to CO_2 and H_2O.

Text S16 Detailed for toxicity assay

To study the detoxification performance of the NPBC900/PDS system, the phytotoxicity tests were conducted on the solution before and after treatment using Chinese cabbage seeds as a model organism. As shown in Fig. S26, the addition of initial SPY significantly inhibited the growth of Chinese cabbage seed root, while the growth of root was promoted with introduction of PDS, which may be due to the acid condition and inorganic salts produced. The L/L_0 was detected as 0.41, 1.93 and 2.36 in the case of SPY, PDS and SPY + PDS + NPBC900, respectively, suggesting that NPBC900/PDS system successfully eliminated the phytotoxicity of SPY and its degradation intermediates, even promote the growth of plants due to the leaching of N, P- element.

Table S1 Relative biochars' surface contents of C1s, O1s, N1s and P2p by XPS spectra curve fitting.

Samples	Surface element composition (%)				Element composition ratio		
	P 2p	C 1s	N 1s	O 1s	N 1s /C 1s	O 1s /C 1s	P 2p /C 1s
BC900	0.97	72.27	2.34	24.42	0.03	0.34	0.01
NPBC900-5:1	3.54	56.62	4.04	35.80	0.07	0.63	0.06
NPBC900-2:1.1	4.62	53.15	2.96	39.27	0.06	0.74	0.09
NPBC900-1:1	1.78	73.75	3.91	20.57	0.05	0.28	0.02
NPBC900-1.1:2	3.31	62.94	4.50	29.25	0.07	0.46	0.05
NPBC900-1:5	3.10	61.57	5.55	29.78	0.09	0.48	0.05

Table S2. Relative biochars' surface contents of C1s, O1s, N1s and P2p by XPS spectra curve fitting.

Samples	Surface element composition (%)				Element composition ratio		
	P 2p	C 1s	N 1s	O 1s	N 1s /C 1s	O 1s /C 1s	P 2p /C 1s
NPBC600	7.61	30.87	3.91	57.61	0.13	1.87	0.25
NPBC700	8.43	25.32	4.55	61.70	0.18	2.44	0.33
NPBC800	6.41	46.80	4.01	42.79	0.09	0.91	0.14
NPBC900	4.62	53.15	2.96	39.27	0.06	0.74	0.09

Table S3. Elemental content, atomic ratio and ash content in biochar samples.

Biochar samples	Element content (%) [a]				Atomic ratio [a]			Ash content [b]
	C	H	O	N	H/C	O/C	(O+N)/C	(%)
BC900	77.67	1.91	18.80	1.61	0.30	0.18	0.20	29.06
NPBC900	64.16	3.00	29.19	1.95	0.55	0.33	0.36	35.84

a Elemental compositions and atomic ratios are on an ash-free basis.

b Ash content was measured by oxidative heating of samples at 750 ºC for 4 h.

Table S4. The kinetic parameters of the adsorption of SPY on biochars.

Samples	Quasi first order equation			Quasi second order equation		
	q_e (mg·g^{-1})	k_1 (min^{-1})	R^2	q_e(mg·g^{-1})	k_2 (g·mg^{-1}·min^{-1})	R^2
NPBC900	12.07 ± 0.46	2.76 ± 0.82	0.950	13.38 ± 0.33	0.01 ± ~0	0.987
BC900	10.66 ± 0.08	2.23 ± 0.36	0.936	11.66 ± 0.31	0.01 ±~0	0.982

Table S5 Parameters for isotherms of SPY adsorption by biochars.

samples	Langmuir model			Freundlich model		
	k_L ($L \cdot mg^{-1}$)	Q_m ($mg \cdot g^{-1}$)	R^2	n	K_f ($mg^{1-n} \cdot g^{-1} \cdot L^n$)	R^2
NPBC900	0.03 ± 0.01	35.14 ± 2.01	0.996	0.61 ± 0.06	2.18 ± 0.48	0.975
BC900	0.05 ± 0.01	27.31 ± 1.84	0.990	0.54± 0.07	2.514 ± 0.66	0.950

Table S6 The specific surface area and pore volume of biochars.

Samples	Surface area ($m^2 \cdot g^{-1}$)	Pore volume ($cm^3 \cdot g^{-1}$)			Average pore diameter (nm)
	S_{BET}	V_{tot}	V_{mic}	V_{meso}	
BC900	414.10	0.328	0.223	0.105	2.16
NPBC900	605.85	0.374	0.155	0.219	3.62

Table S7 Removal efficiency of SAs by different methods of PDS activation.

Reaction system	Reaction conditions	Antibiotic	Removal efficiency	Ref.
Fe^{2+}/PDS	PDS=1.0 mmol/L，Fe^{2+}= 0.5 mmol/L	Sulfaquinoxaline (30 μmol/L)	40.9%	Ji et al., 2017
Co^{2+}/PDS/ACF	PDS=5 mmol/L, Co^{2+}=1.0 mmol/L	sulfamethoxazole (0.02 mmol/L)	65.6%	Liu et al., 2020
H_2O_2/PDS	PDS=20 mmol/L, $H_2O_{2=}$10 mmol/L	Sulfapyridine （10 mg/L）	88.9%	Yao et al., 2021
UV/PDS	PDS=1 mmol/L, UV fluence=900 mJ cm^{-2}	Sulfasalazine (29.1 μmol/L)	96.2%	Ji et al., 2018
Fe/Cu-biochar/PDS	PDS=4 mmol/L, Fe/Cu-biochar =1 g/L	Sulfapyridine （20 mg/L）	97.6%	Cai et al., 2020
NPBC900/PDS	PDS=0.5 mmol/L, NPBC900=0.1 g/L	Sulfapyridine （20 mg/L）	98.3%	In this study

Table S8 Relative biochars' surface contents of C1s, O1s, N1s and P2p by XPS spectra curve fitting.

Samples	Surface element composition (%)				Element composition ratio		
	P 2p	C 1s	N 1s	O 1s	N 1s /C 1s	O 1s /C 1s	P 2p /C 1s
NPBC900	4.62	53.15	2.96	39.27	0.06	0.74	0.09
NPBC900 -used	0.81	58.20	7.81	33.18	0.13	0.57	0.01

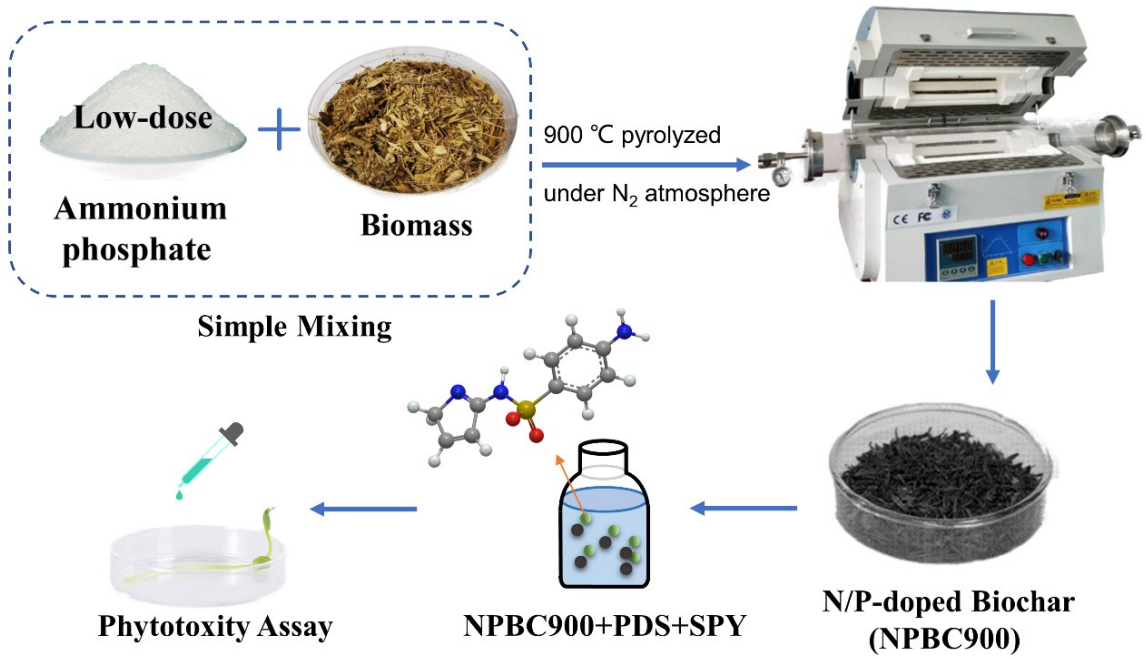

Fig. S1. Schematic illustration of NPBC900 synthesis for sulfapyridine (SPY) removal and the toxicity test for degradation intermediates.

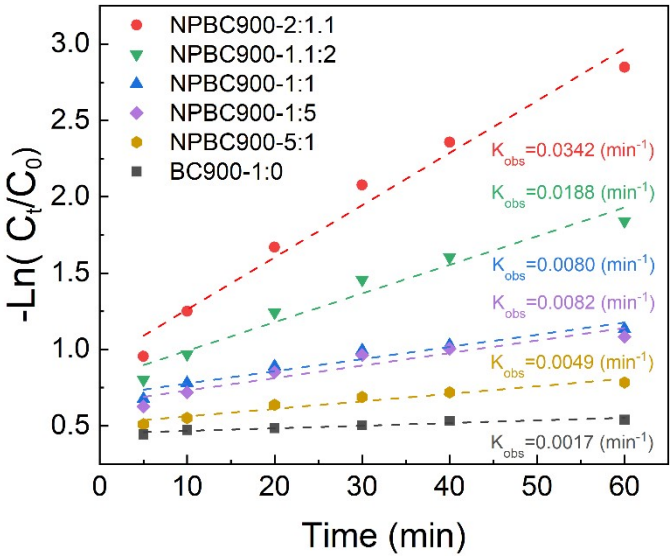

Fig. S2. The k_{obs} value of NPBC synthesized with different proportions of biomass and APP in AOPs.

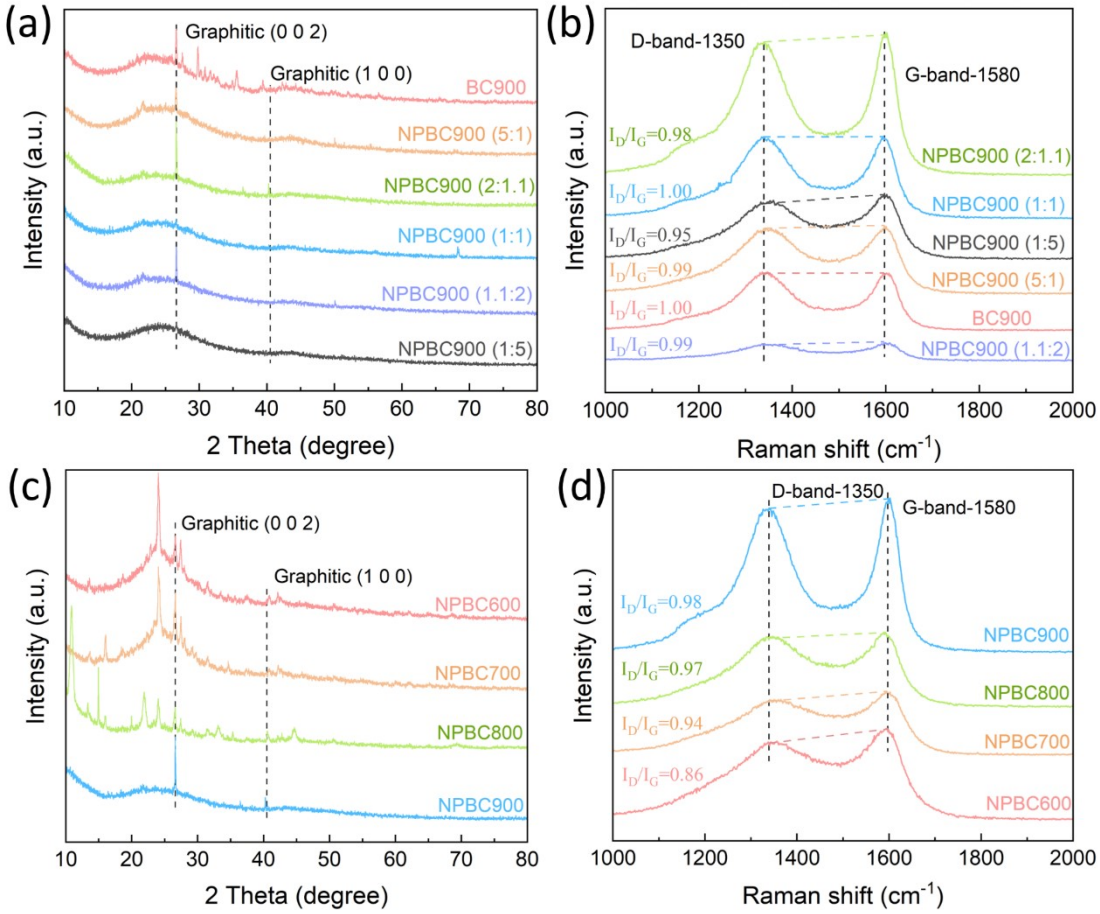

Fig. S3. The XRD (a, c) and Raman (b, d) spectra of NPBC.

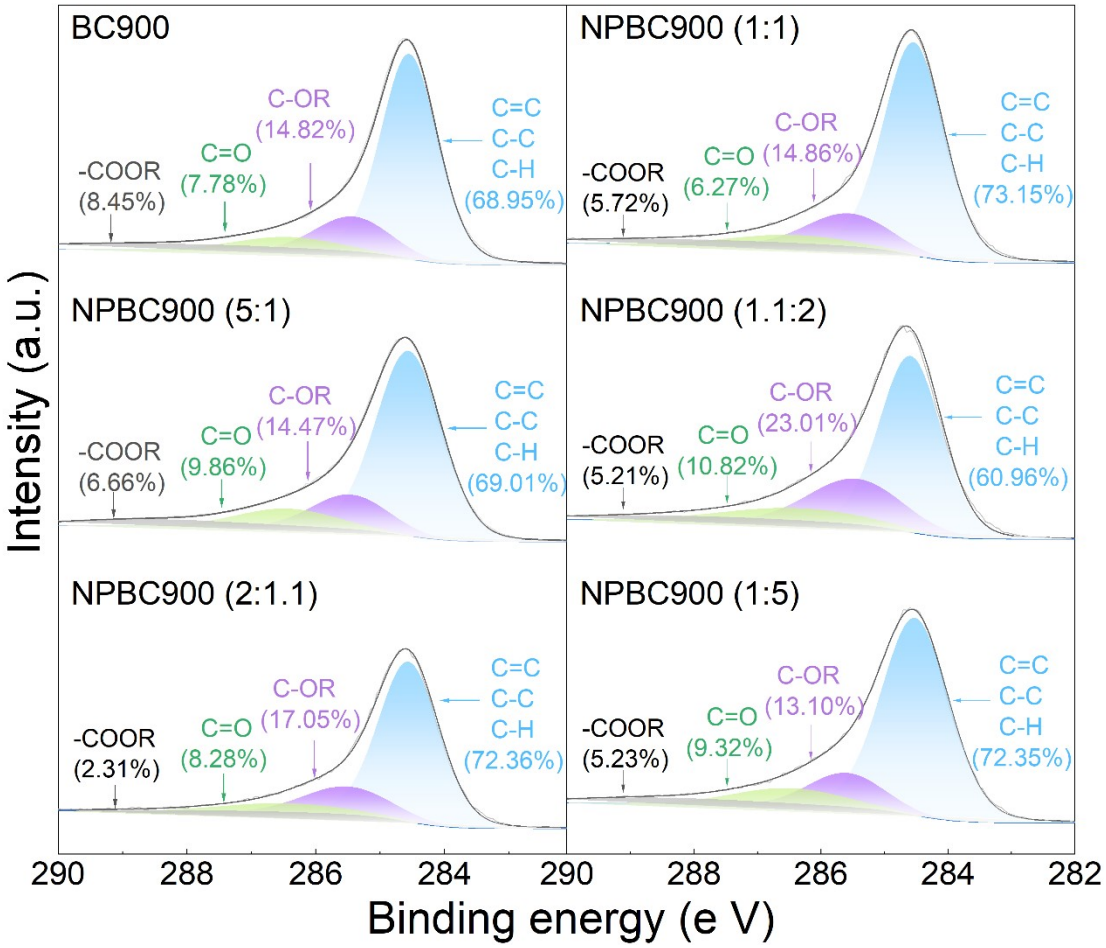

Fig. S4. The XPS spectra of C 1s of NPBC synthesized with different proportions of biomass and APP.

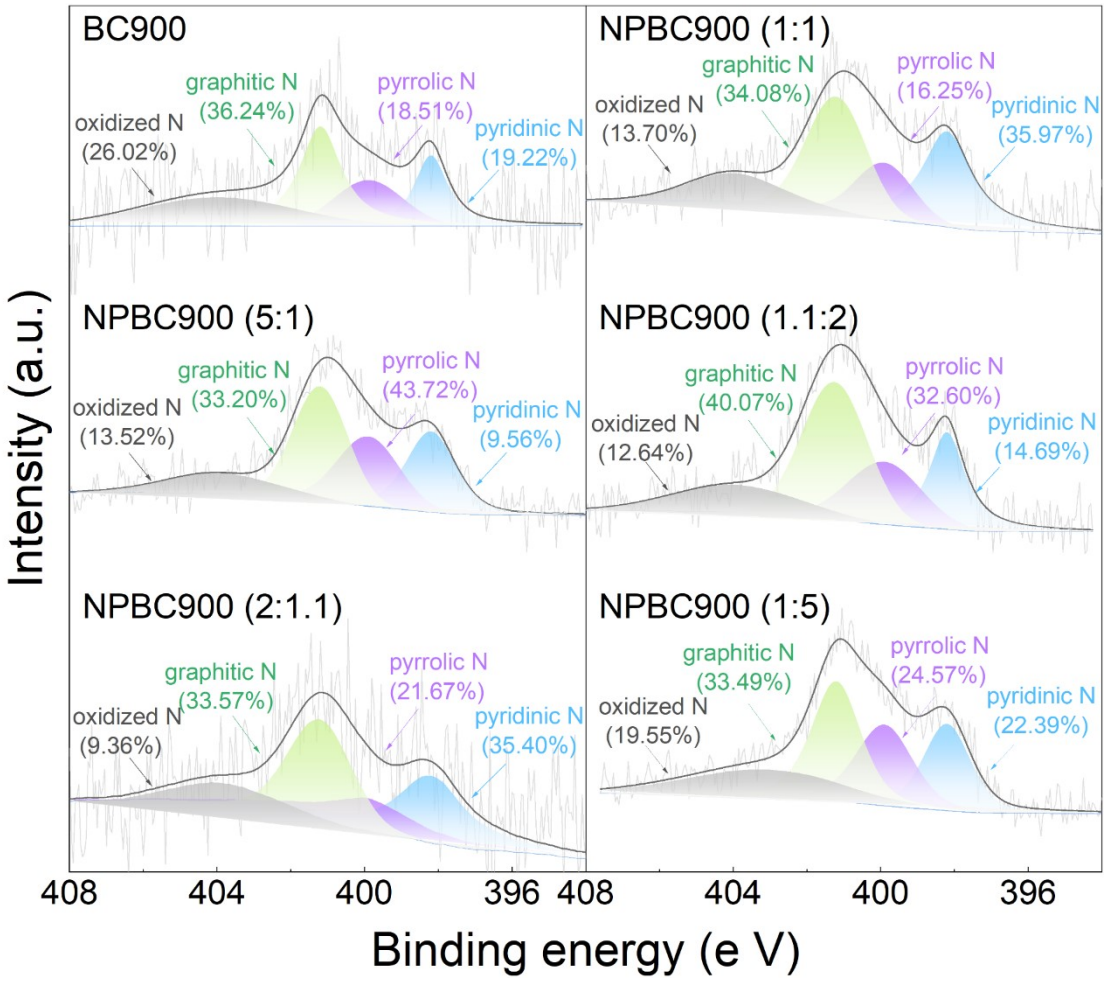

Fig. S5. The XPS spectra of N 1s of NPBC synthesized with different proportions of biomass and APP.

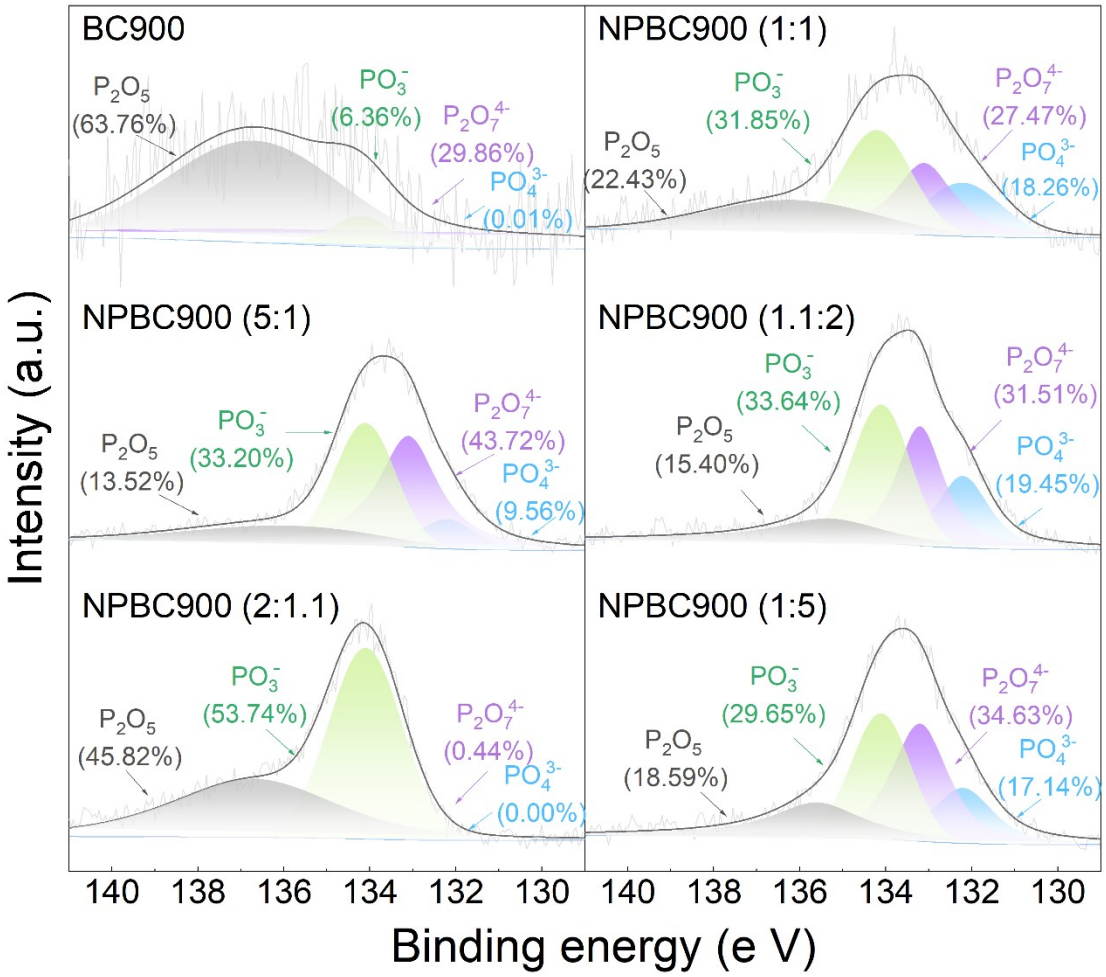

Fig. S6. The XPS spectra of P 2p of NPBC synthesized with different proportions of biomass and APP.

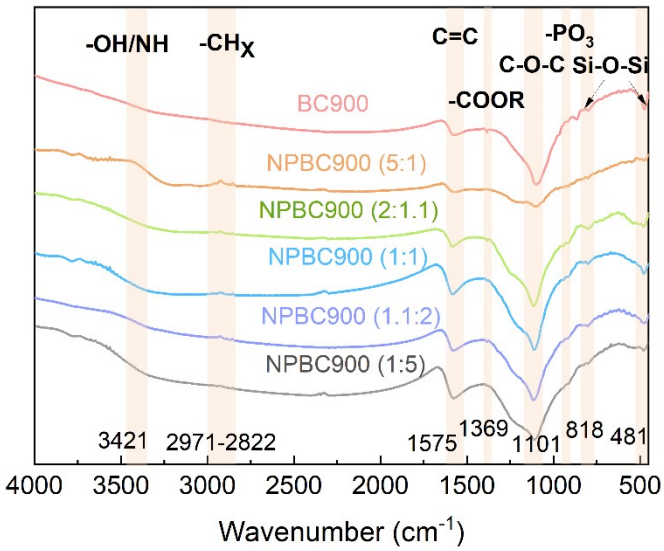

Fig. S7. The FTIR spectra of NPBC synthesized with different proportions of biomass and APP.

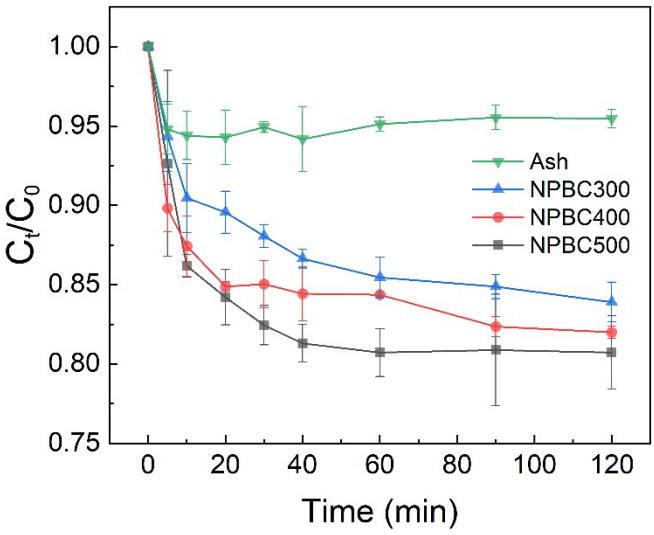

Fig. S8. PDS activation for SPY removal by NPBC synthesized with low pyrolysis temperature.

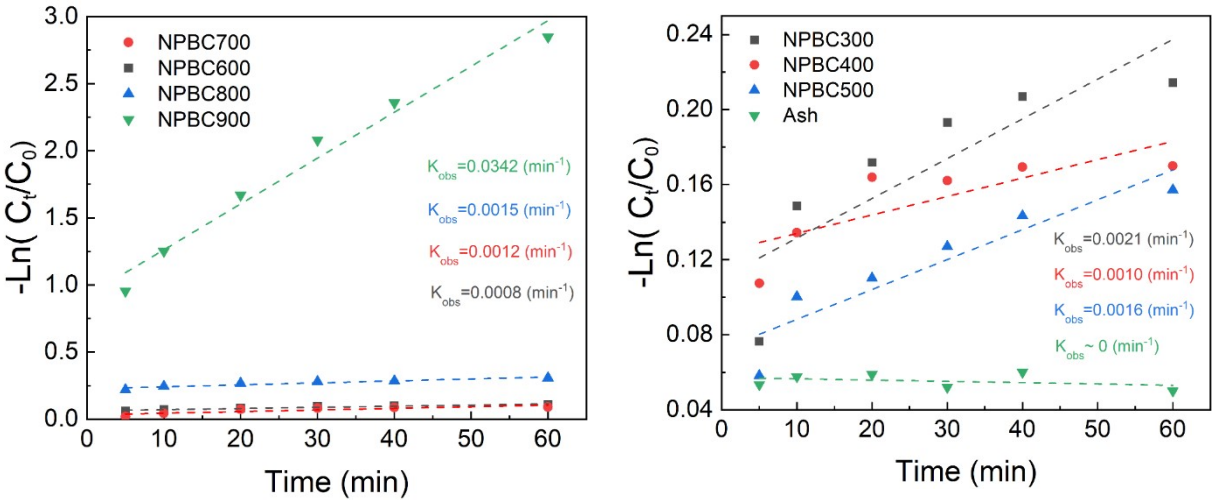

Fig. S9. The k_{obs} value of NPBC synthesized with different pyrolysis temperature.

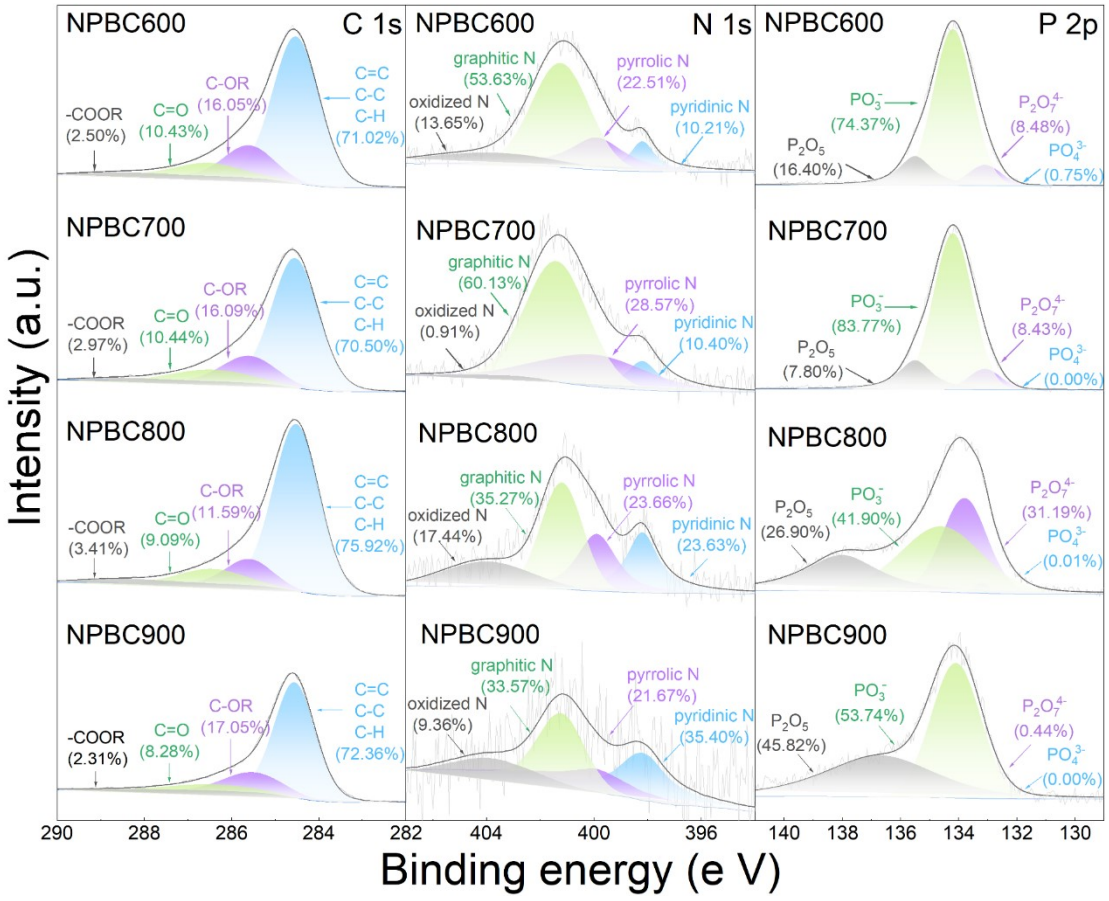

Fig. S10. The XPS spectra of NPBC synthesized with high pyrolysis temperature.

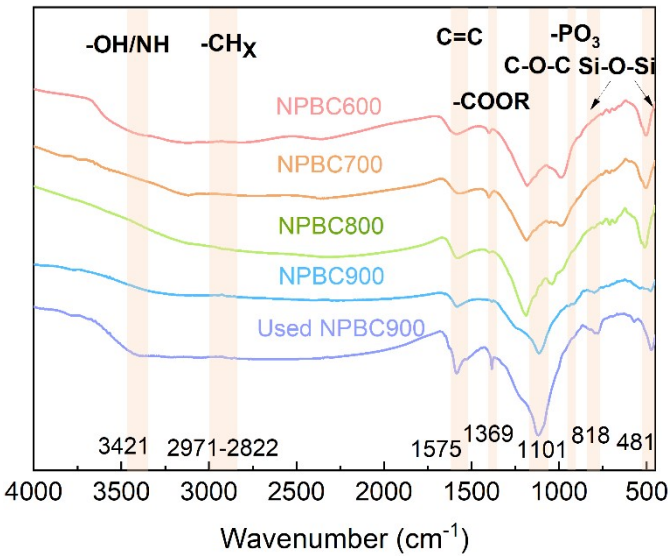

Fig. S11. The FTIR spectra of NPBC synthesized with high pyrolysis temperature and used NPBC900.

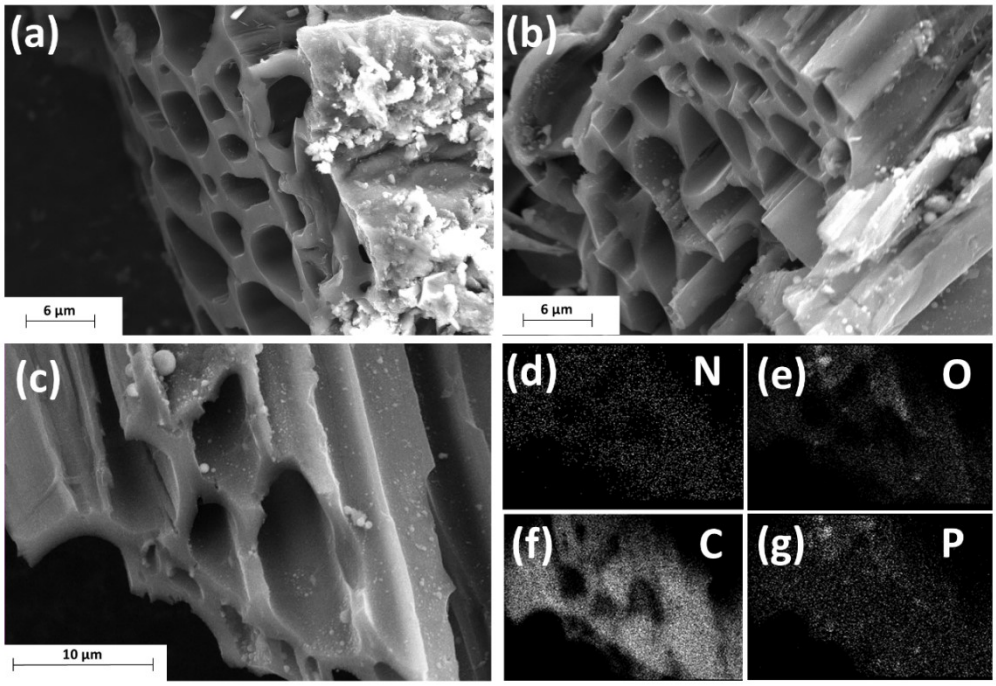

Fig. S12. SEM images of pristine biochar BC900(a) and N, P-co-doped biochar NPBC900 (b, c); Elemental maps of NPBC900 (d-g).

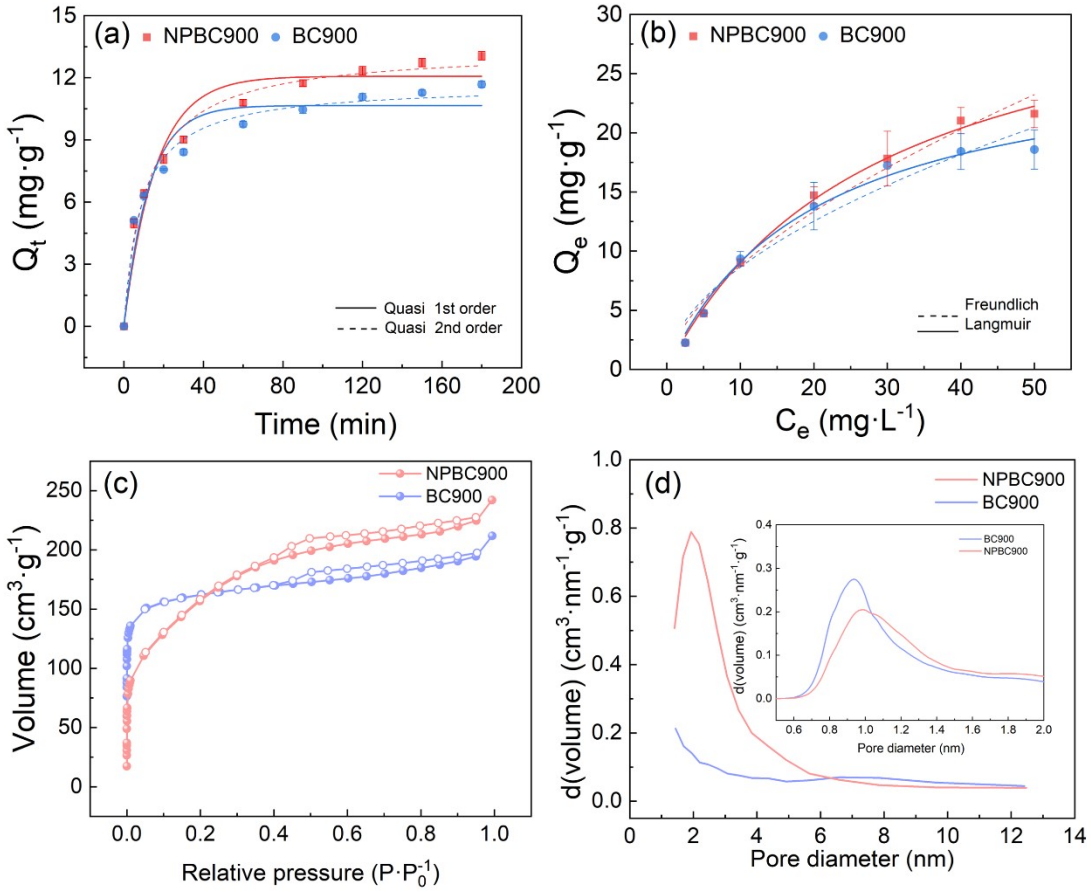

Fig. S13. SPY adsorption kinetics (a) and adsorption isotherms (b) for pristine and modified biochars (SPY=0~50 mg L^{-1}, Catalyst=0.1 g L^{-1}, initial solution pH=6.71); The N_2 adsorption-desorption isotherms of biochars (c), the meso-pores and micro-pores distribution of biochars (d).

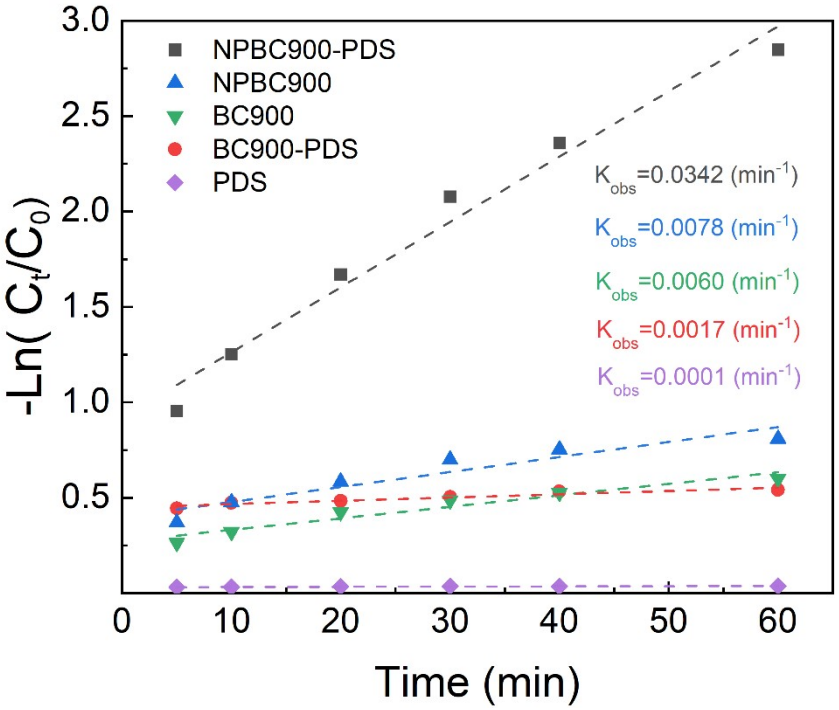

Fig. S14. The k_{obs} value of different degradation systems.

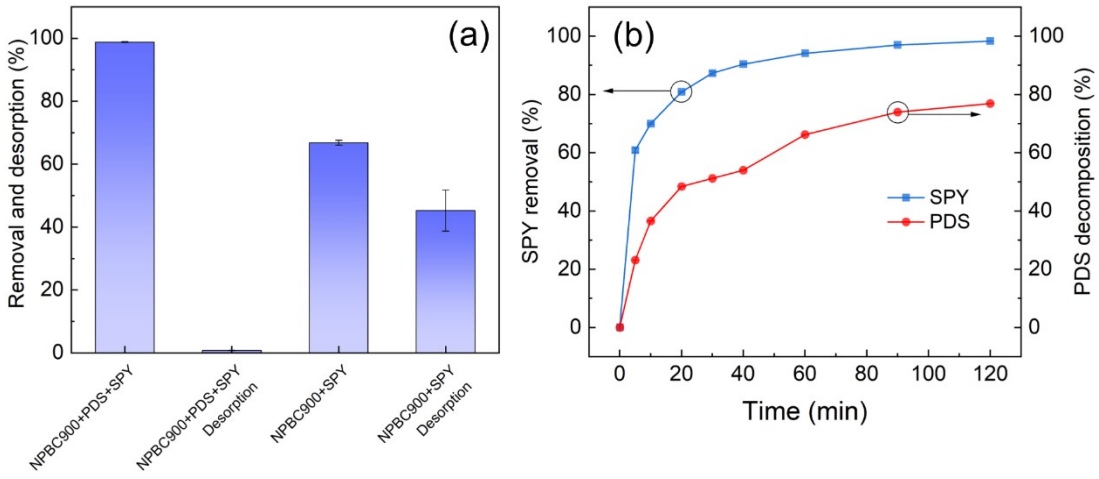

Fig. S15. The desorption of SPY (a) and the correlation of SPY removal and PDS decomposition (b).

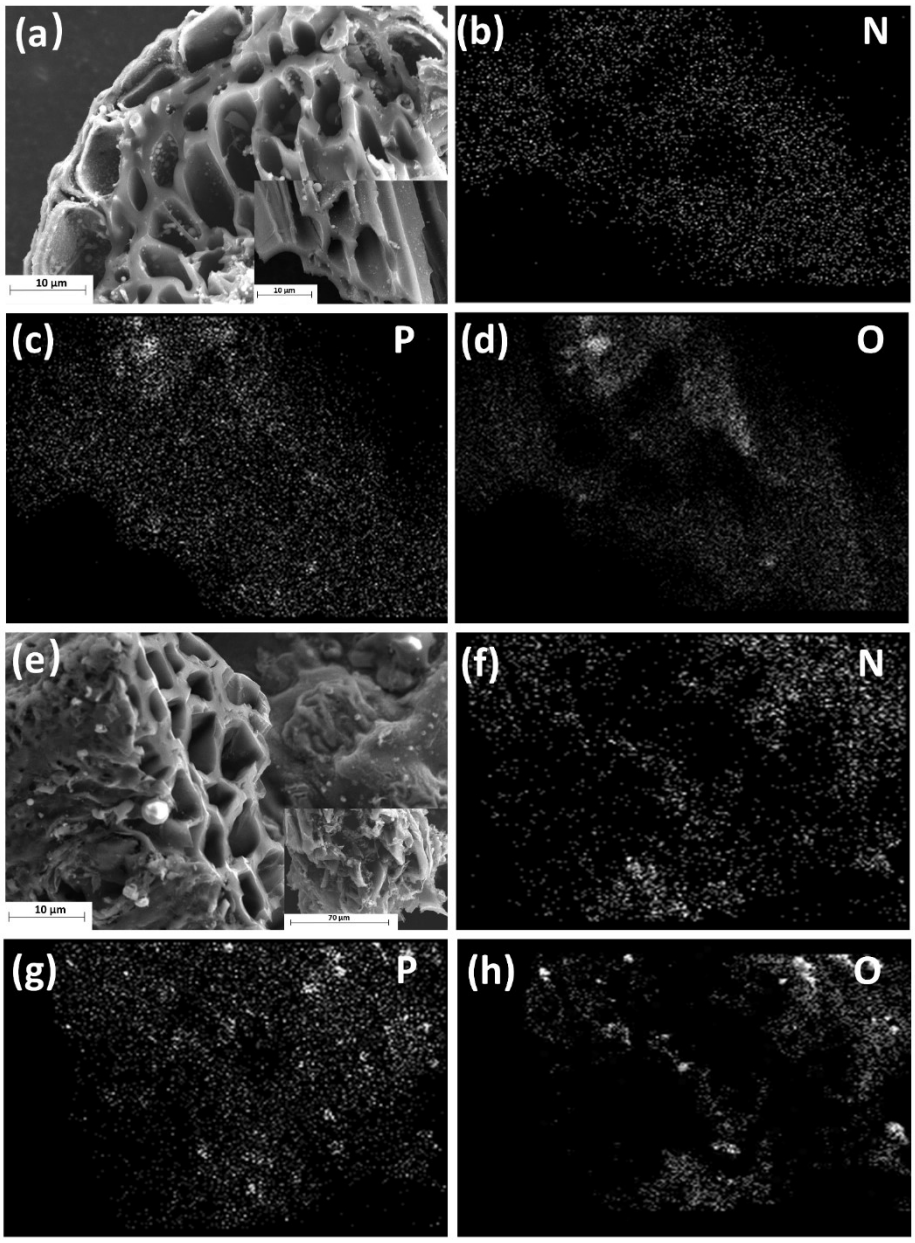

Fig. S16. The SEM-EDS images of NPBC900 before and after used (a, e) and the element distribution mapping of O, N, P in NPBC900 (b-d, f-h).

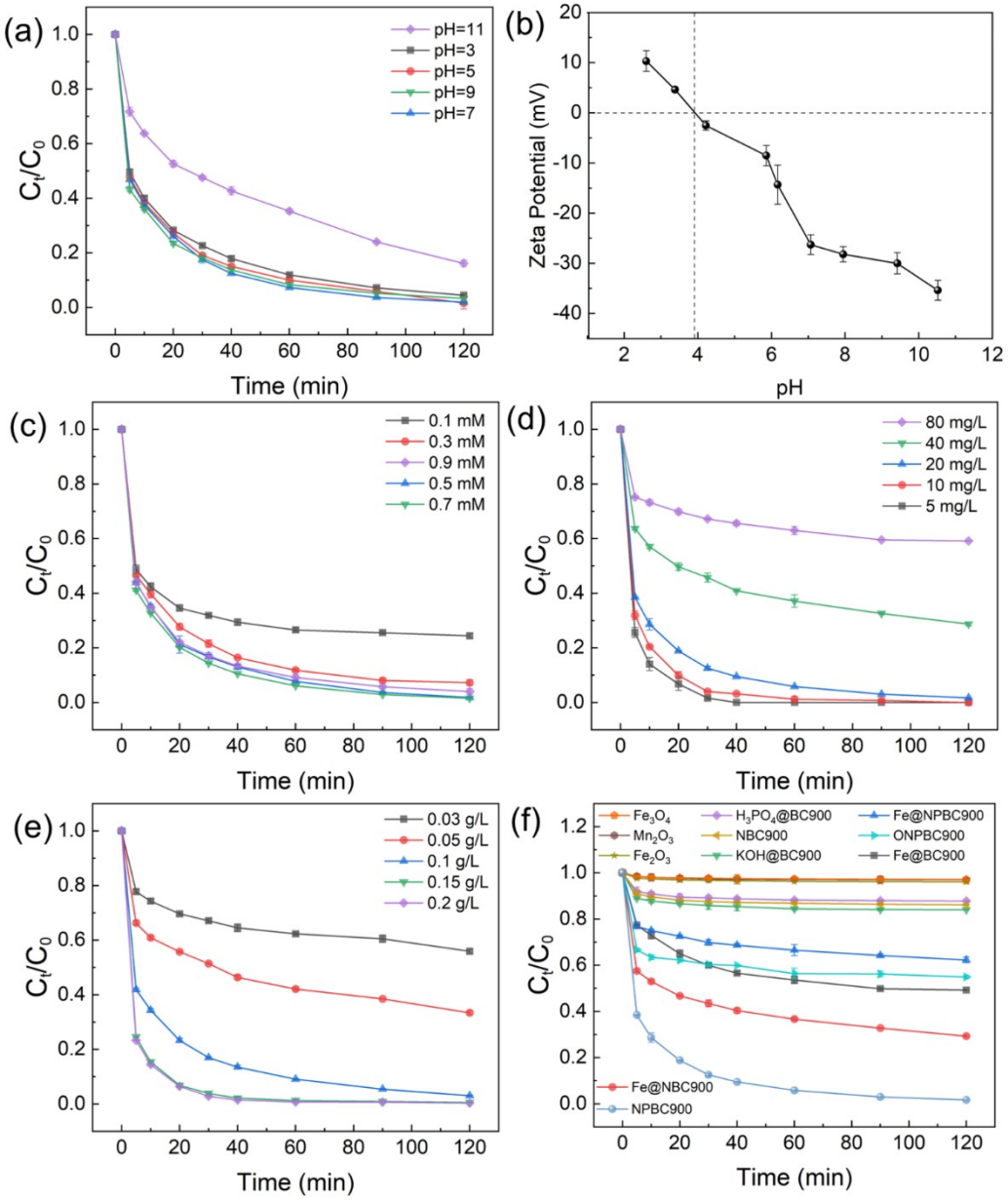

Fig. S17. Effects of solution pH (a), Zeta potential of NPBC900 (b), PDS concentration (c), SPY initial concentration (d), NPBC900 dosage (e), comparison of common catalysts on PDS activation performance for SPY removal (f). (Reaction conditions: SPY=20 mg L^{-1}, PDS=0.5 mM, Catalyst=0.1 g L^{-1}, initial solution pH=6.71.)

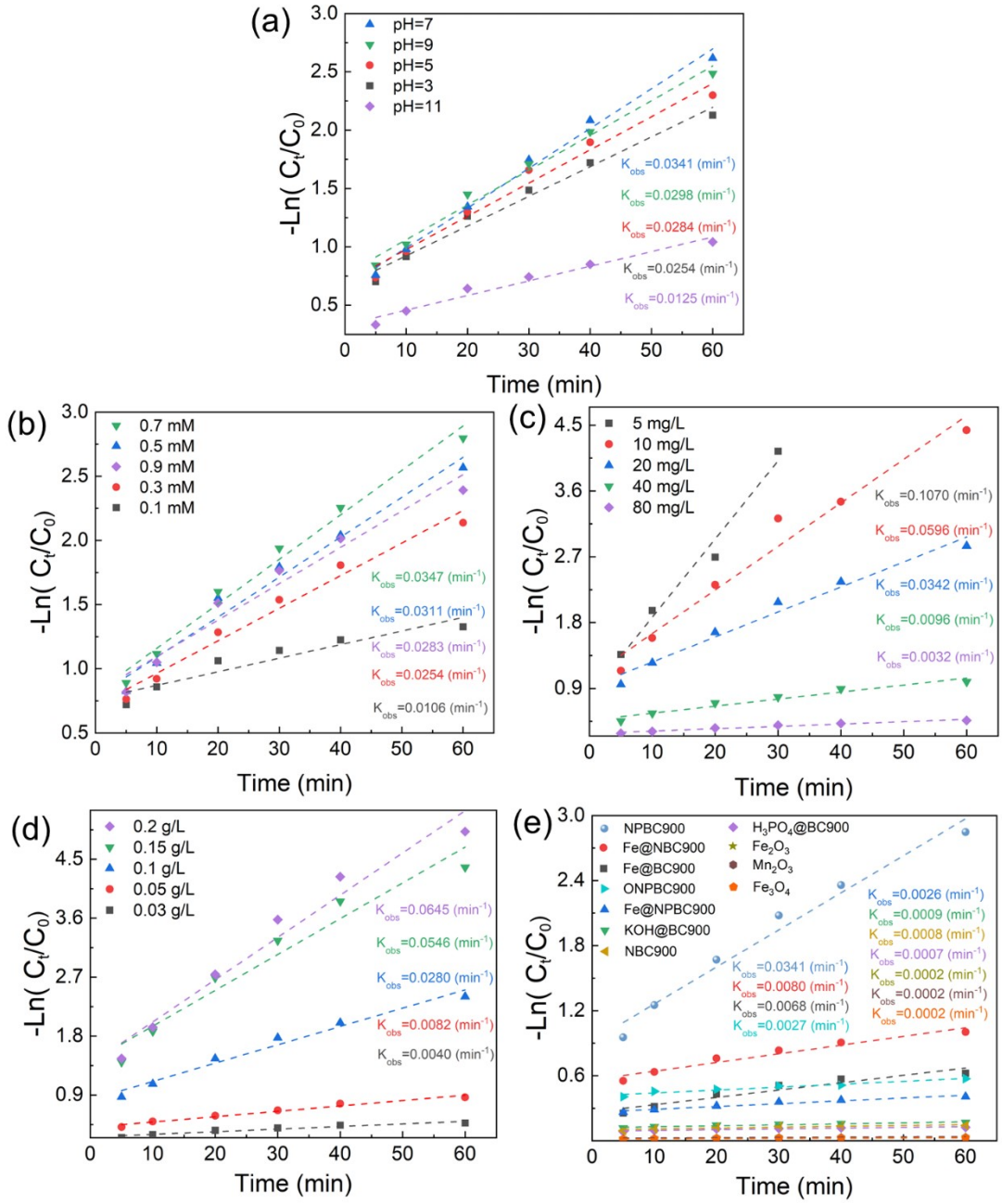

Fig. S18. The k_{obs} value of different reaction conditions on SPY removal.

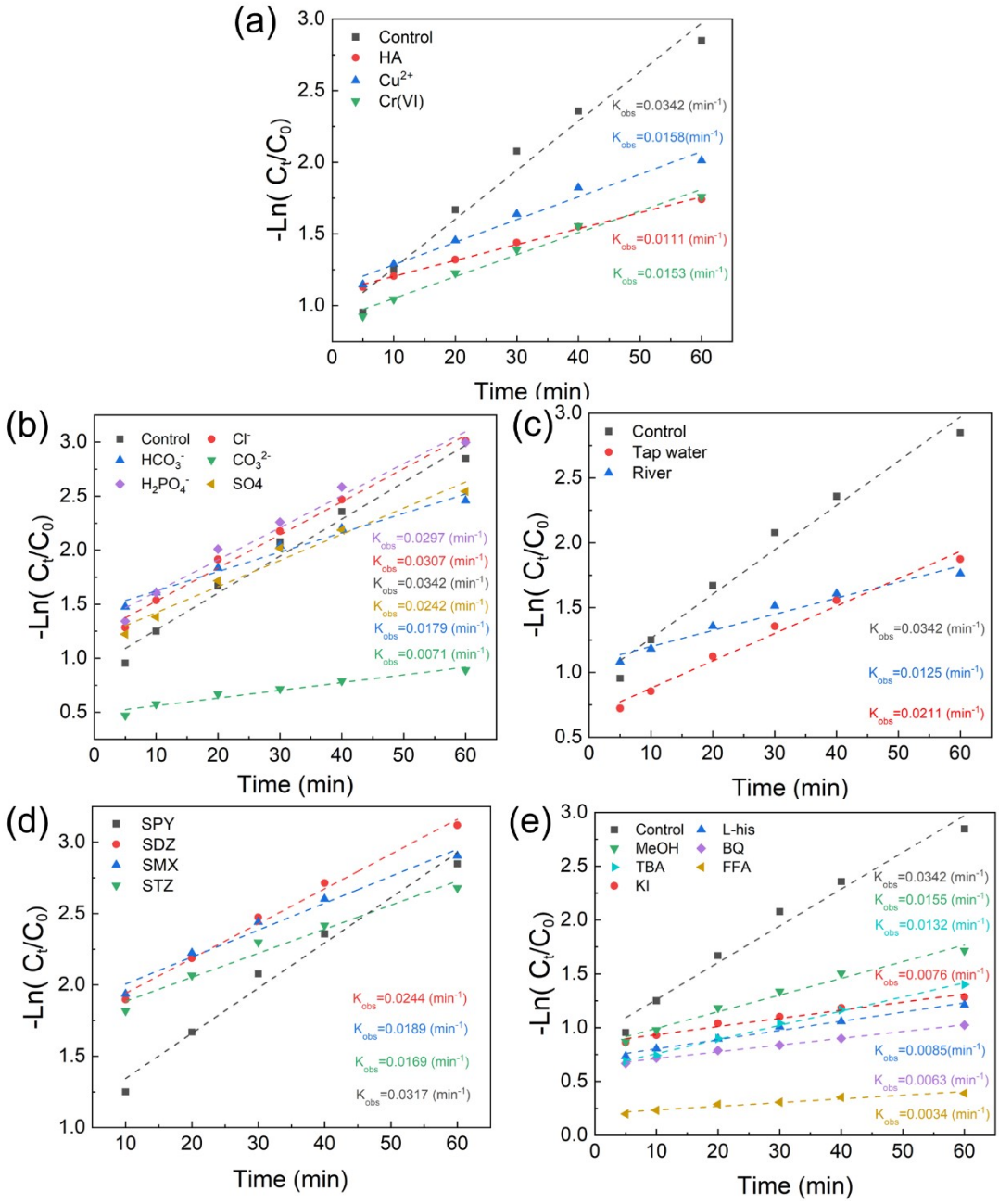

Fig. S19. The k_{obs} value of another reaction conditions on SPY removal.

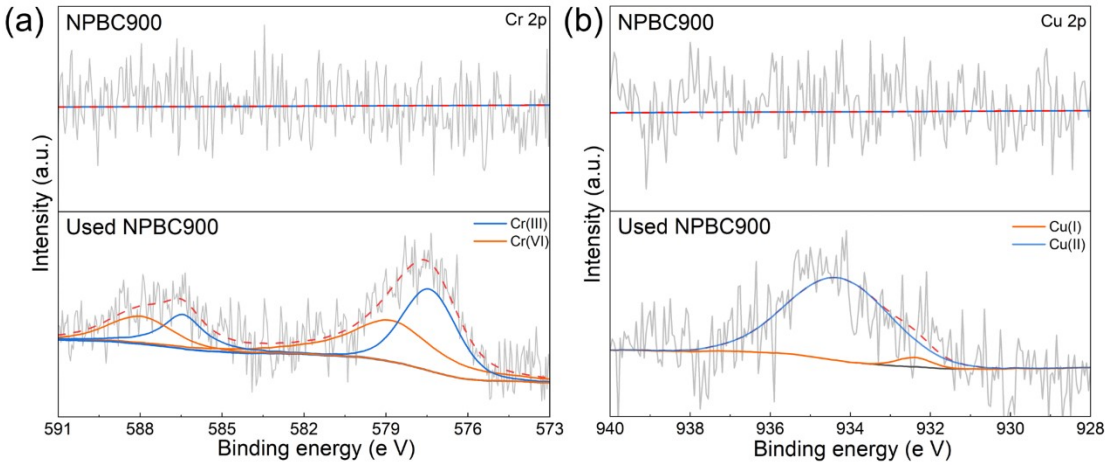

Fig. S20. Fitted curves for Cu 2p/Cr 2p spectra of NPBC900, before and after SPY removal with coexisting Cu^{2+} or Cr (VI).

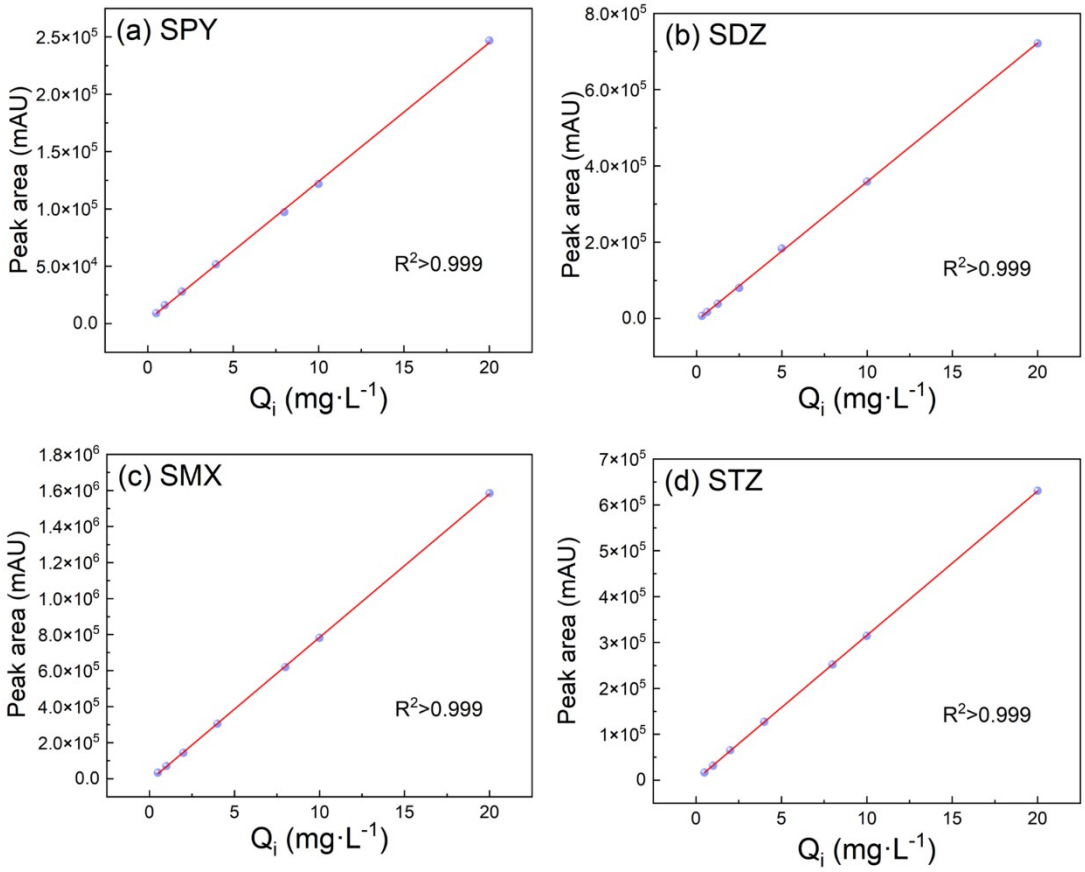

Fig. S21. The standard line test of SAs.

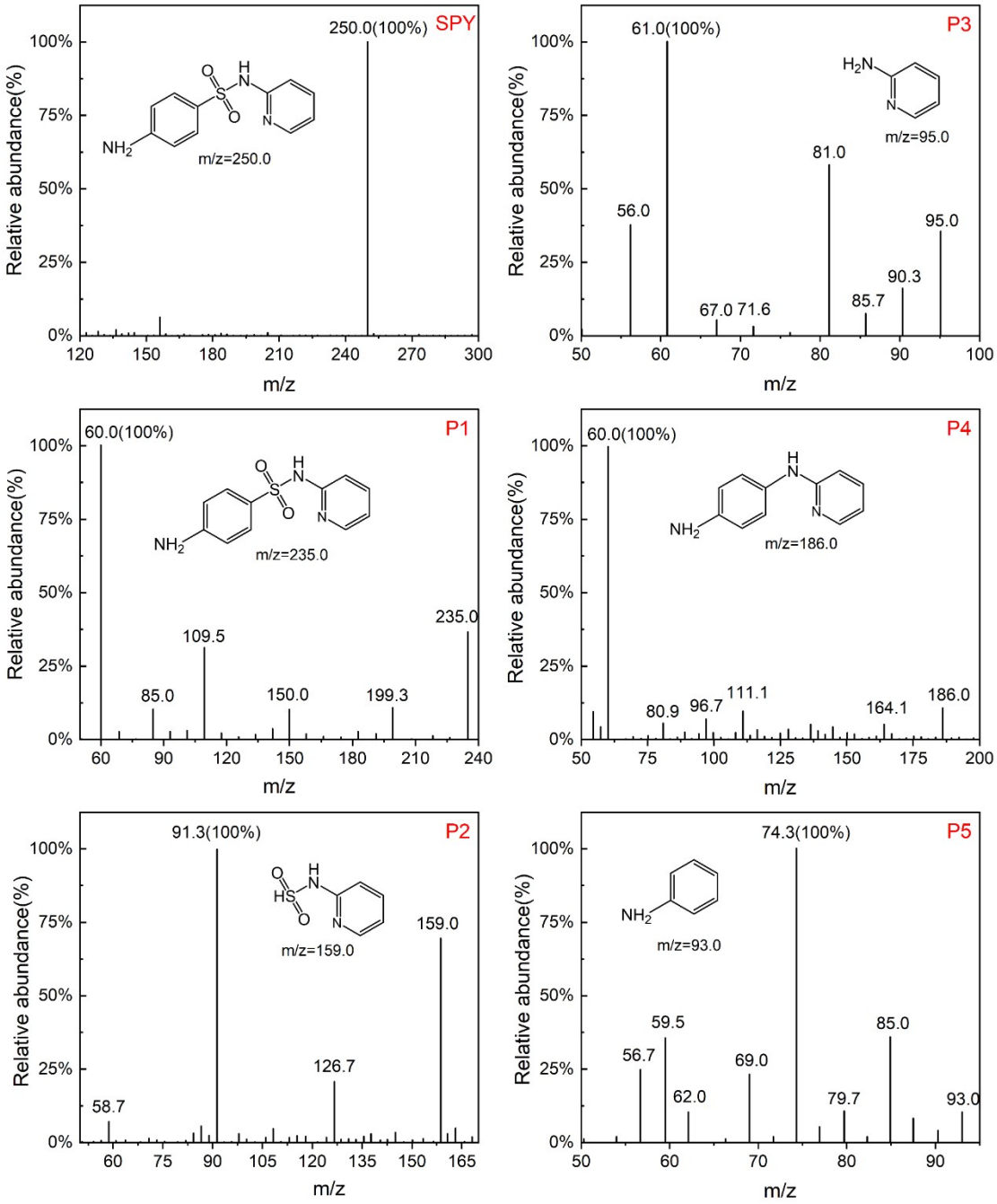

Fig. S22. The MS spectrum of SPY and P1-5.

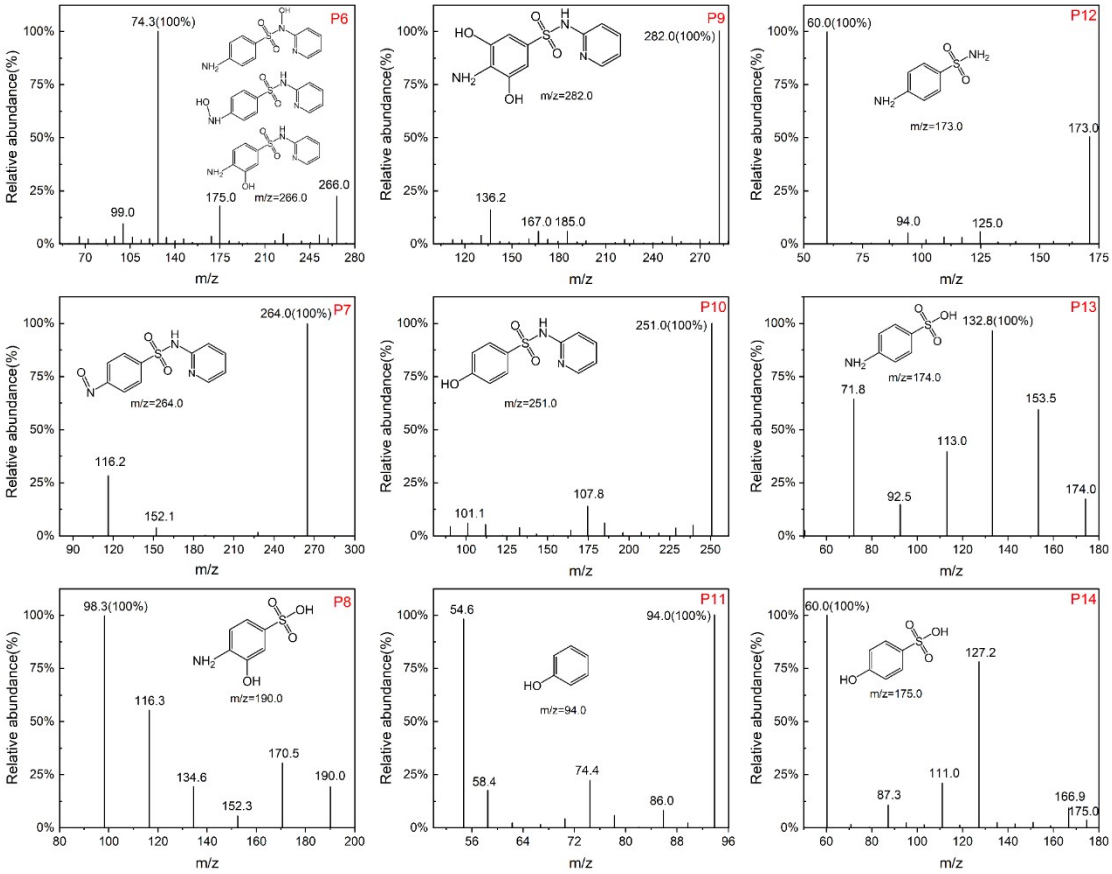

Fig. S23. The MS spectrum of P6 to 14.

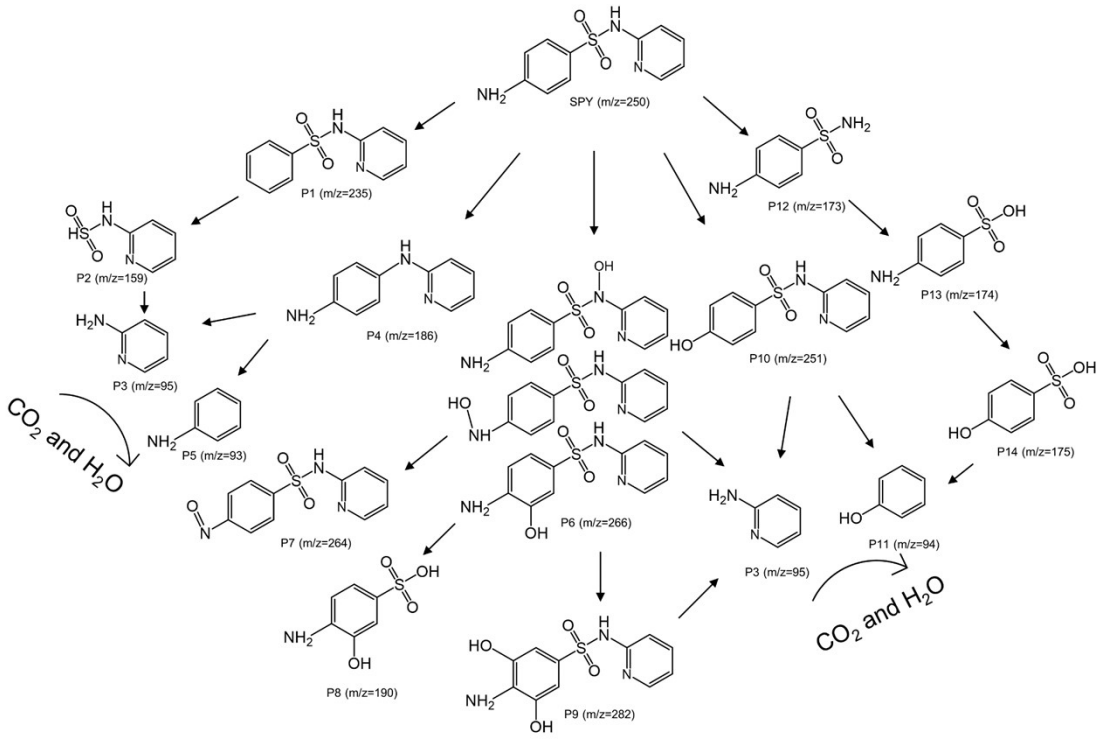

Fig. S24. Proposed SPY degradation pathways in the NPBC900/PDS system

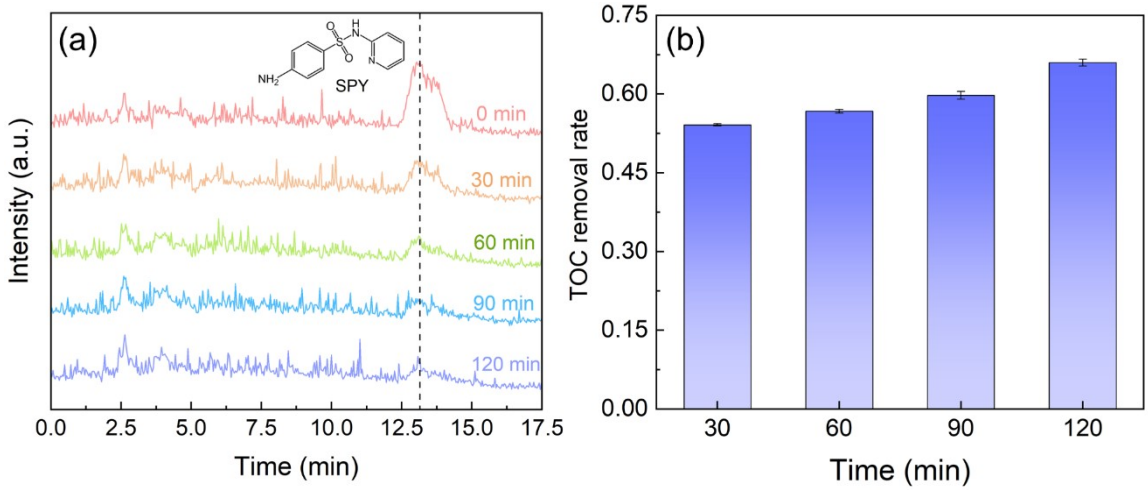

Fig. S25. The chromatogram of SPY by ESI-MS(a) and TOC removal by the NPBC900/PDS systems.

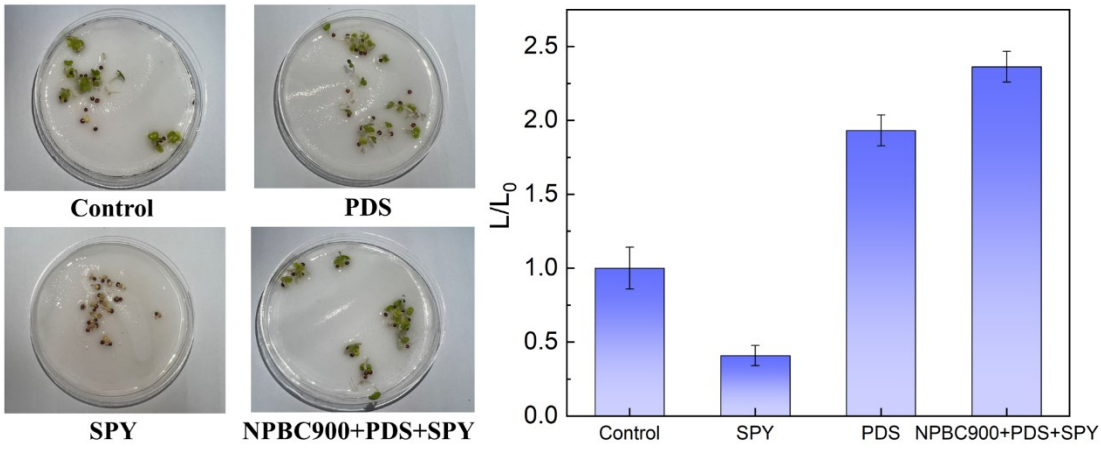

Fig. S26. The phytotoxicity of SPY, PDS, SPY treated by NPBC900/PDS system on Chinese cabbage seeds, and L/L_0 of Chinese cabbage seeds under different conditions.

References

Cai, S., Liu, Y., Chen, J., 2020. FeCu-biochar enhances the removal of antibacterial sulfapyridine from groundwater by activation of persulfate. Environmental Chemistry Letters, 18(5), 1693-1700.

Deng, Y., Zhou, Z., Zeng, H., Tang, R., Li, L., Wang, J., ... & Huang, Y. (2023). Phosphorus and kalium co-doped g-C_3N_4 with multiple-locus synergies to degrade atrazine: Insights into the depth analysis of the generation and role of singlet oxygen. Applied Catalysis B: Environmental, 320, 121942.

Ding, D., Zhao, Y., Yang, S., Shi, W., Zhang, Z., Lei, Z., & Yang, Y. (2013). Adsorption of cesium from aqueous solution using agricultural residue–walnut shell: equilibrium, kinetic and thermodynamic modeling studies. Water Research, 47(7), 2563-2571.

Gao, J., & Pedersen, J. A. (2005). Adsorption of sulfonamide antimicrobial agents to clay minerals. Environmental Science & Technology, 39(24), 9509-9516.

Guo, Y., Zeng, Z., Zhu, Y., Huang, Z., Cui, Y., & Yang, J. (2018). Catalytic oxidation of aqueous organic contaminants by persulfate activated with sulfur-doped hierarchically porous carbon derived from thiophene. Applied Catalysis B: Environmental, 220, 635-644.

Guizani, C., Haddad, K., Limousy, L., & Jeguirim, M. (2017). New insights on the structural evolution of biomass char upon pyrolysis as revealed by the Raman spectroscopy and elemental analysis. Carbon, 119, 519-521.

Huang, C., Puziy, A. M., Sun, T., Poddubnaya, O. I., Suárez-García, F., Tascón, J. M., & Hulicova-Jurcakova, D. (2014). Capacitive behaviours of phosphorus-rich carbons derived from

lignocelluloses. Electrochimica Acta, 137, 219-227.

Ji, Y., Wang, L., Jiang, M., Yang, Y., Yang, P., Lu, J., Ferronato, C., & Chovelon, J. M., 2017. Ferrous-activated peroxymonosulfate oxidation of antimicrobial agent sulfaquinoxaline and structurally related compounds in aqueous solution: kinetics, products, and transformation pathways. Environmental Science and Pollution Research, 24(24), 19535-19545.

Ji, Y., Yang, Y., Zhou, L., Wang, L., Lu, J., Ferronato, C., Chovelon, J. M., 2018. Photodegradation of sulfasalazine and its human metabolites in water by UV and UV/peroxydisulfate processes. Water Research, 133, 299-309.

Liu, S., Hassan, S. U., Ding, H., Li, S., Jin, F., Miao, Z., Wang, X., Li, H., Zhao, C., 2020a. Removal of sulfamethoxazole in water by electro-enhanced Co^{2+}/peroxydisulfate system with activated carbon fiber-cathode. Chemosphere, 245, 125644.

Liu, S., Zhao, C., Wang, Z., Ding, H., Deng, H., Yang, G., ... & Zheng, H. (2020b). Urea-assisted one-step fabrication of a novel nitrogen-doped carbon fiber aerogel from cotton as metal-free catalyst in peroxymonosulfate activation for efficient degradation of carbamazepine. Chemical Engineering Journal, 386, 124015.

Pang, K., Sun, W., Ye, F., Yang, L., Pu, M., Yang, C., ... & Niu, J. (2022). Sulfur-modified chitosan derived N, S-co-doped carbon as a bifunctional material for adsorption and catalytic degradation sulfamethoxazole by persulfate. Journal of Hazardous Materials, 424, 127270.

Parab, H., & Sudersanan, M. (2010). Engineering a lignocellulosic biosorbent–coir pith for removal of cesium from aqueous solutions: equilibrium and kinetic studies. Water Research, 44(3), 854-860.

Shih, P. Y., Yung, S. W., & Chin, T. S. (1999). FTIR and XPS studies of P_2O_5–Na_2O–CuO glasses. Journal of non-crystalline solids, 244(2-3), 211-222.

Tang, W., Zanli, B. L. G. L., & Chen, J. (2021). O/N/P-doped biochar induced to enhance adsorption of sulfonamide with coexisting Cu^{2+}/Cr (VI) by air pre-oxidation. Bioresource Technology, 341, 125794.

Yao, P., Chen, L., Zhang, Y., & Wen, D., 2021. The pre-oxidation kinetics and mechanism of sulfapyridine for biodegradability improvement. Journal of Cleaner Production, 329, 129698.

Yin, R., Guo, W., Wang, H., Du, J., Wu, Q., Chang, J. S., & Ren, N. (2019). Singlet oxygen-dominated peroxydisulfate activation by sludge-derived biochar for sulfamethoxazole degradation through a nonradical oxidation pathway: Performance and mechanism. Chemical Engineering Journal, 357, 589-599.